J. Fluid Mech. (2014), *vol.* 756, *pp.* 555–599. © Cambridge University Press 2014
doi:10.1017/jfm.2014.412

Dense shallow granular flows

V. Kumaran[1,†]

[1]Department of Chemical Engineering, Indian Institute of Science, Bangalore 560 012, India

(Received 12 February 2014; revised 27 June 2014; accepted 16 July 2014;
first published online 3 September 2014)

Simplified equations are derived for a granular flow in the 'dense' limit where the volume fraction is close to that for dynamical arrest, and the 'shallow' limit where the stream-wise length for flow development (L) is large compared with the cross-stream height (h). The mass and diameter of the particles are set equal to 1 in the analysis without loss of generality. In the dense limit, the equations are simplified by taking advantage of the power-law divergence of the pair distribution function χ proportional to $(\phi_{ad}-\phi)^{-\alpha}$, and a faster divergence of the derivative $\rho(\mathrm{d}\chi/\mathrm{d}\rho) \sim (\mathrm{d}\chi/\mathrm{d}\phi)$, where ρ and ϕ are the density and volume fraction, and ϕ_{ad} is the volume fraction for arrested dynamics. When the height h is much larger than the conduction length, the energy equation reduces to an algebraic balance between the rates of production and dissipation of energy, and the stress is proportional to the square of the strain rate (Bagnold law). In the shallow limit, the stress reduces to a simplified Bagnold stress, where all components of the stress are proportional to $(\partial u_x/\partial y)^2$, which is the cross-stream (y) derivative of the stream-wise (x) velocity. In the simplified equations for dense shallow flows, the inertial terms are neglected in the y momentum equation in the shallow limit because the are $O(h/L)$ smaller than the divergence of the stress. The resulting model contains two equations, a mass conservation equations which reduces to a solenoidal condition on the velocity in the incompressible limit, and a stream-wise momentum equation which contains just one parameter $\mathscr{B}$ which is a combination of the Bagnold coefficients and their derivatives with respect to volume fraction. The leading-order dense shallow flow equations, as well as the first correction due to density variations, are analysed for two representative flows. The first is the development from a plug flow to a fully developed Bagnold profile for the flow down an inclined plane. The analysis shows that the flow development length is $(\bar{\rho}h^3/\mathscr{B})$, where $\bar{\rho}$ is the mean density, and this length is numerically estimated from previous simulation results. The second example is the development of the boundary layer at the base of the flow when a plug flow (with a slip condition at the base) encounters a rough base, in the limit where the momentum boundary layer thickness is small compared with the flow height. Analytical solutions can be found only when the stream-wise velocity far from the surface varies as x^F, where x is the stream-wise distance from the start of the rough base and F is an exponent. The boundary layer thickness increases as $(l^2x)^{1/3}$ for all values of F, where the length scale $l=\sqrt{2\mathscr{B}/\bar{\rho}}$. The analysis reveals important differences between granular flows and the flows of Newtonian fluids. The Reynolds number (ratio of inertial and viscous terms) turns out to depend only on the layer height and Bagnold coefficients, and is independent of the flow velocity, because both the inertial terms in the conservation equations and the divergence of the stress depend on the square of the velocity/velocity gradients.

†Email address for correspondence: kumaran@chemeng.iisc.ernet.in

https://doi.org/10.1017/jfm.2014.412 Published online by Cambridge University Press

The compressibility number (ratio of the variation in volume fraction and mean volume fraction) is independent of the flow velocity and layer height, and depends only on the volume fraction and Bagnold coefficients.

Key words: complex fluids, granular media

1. Introduction

Many natural phenomena such as avalanches and land slides, as well as industrial applications involving solids transport and handling, are difficult to model and predict due to a lack of a hydrodynamic description of dense granular flows. The purpose of the present analysis is to formulate dynamical equations for granular flows which are dense (where momentum and energy transport occur primarily due to particle collisions) and shallow (where the stream-wise length scale for flow development is much larger than the cross-stream thickness).

Granular materials are dissipative systems where thermal fluctuations are negligible due to the macroscopic size of the grains, and interactions between the constituent particles result in a dissipation of energy. Due to this, a constant supply of energy is required to 'fluidise' the particles and to facilitate flow. This is in contrast to normal fluids where the thermal fluctuations facilitate molecular motion and fluid deformation. The source of energy could be either through forcing at the boundaries or due internal sources such as shear. The methods of statistical mechanics usually used for deriving constitutive relations for near-equilibrium systems cannot be directly applied to granular flows. In addition, the scale separation between the particle scale and the macroscopic flow scale in granular flows is much smaller than that between the molecular and flow scales in molecular fluids. Due to this, non-continuum effects are often important. The description of dense granular flows is further complicated when the volume fraction is close to the random close packing (RCP) volume fraction, where a simple statistical averaging over pairs of particle interactions may not be sufficient, and it is necessary to incorporate particle correlations.

Granular dynamics in the collisional regime has been studied quite extensively starting from the Boltzmann and Enskog equations for inelastic particle systems. In the dilute limit, conservation equations and constitutive relations are derived which are similar to the Navier–Stokes mass, momentum and energy equations, with the important difference that the energy equation contains an energy dissipation term due to inelastic collisions (Savage & Jeffrey 1981; Jenkins & Savage 1983; Lun *et al.* 1984; Jenkins & Richman 1985; Kumaran 1998). In addition to the standard expansion in the gradients of the macroscopic fields, systematic asymptotic expansions using the inelasticity as a small parameter have been used to derive the constitutive relations up to the second (Burnett) order in the expansion (Sela, Goldhirsch & Noskowicz 1996; Sela & Goldhirsch 1998; Kumaran 2004, 2006*a*). The constitutive equations have been used to study diverse systems such as the homogeneous cooling state where an initial homogeneously agitated granular state 'cools' due to inelastic collisions, vibrated granular beds where there is a source due to a vibrating bottom surface (Kumaran 1998; Soto, Mareschal & Risso 1999; Brey, Ruiz-Montero & Moreno 2001), and sheared granular flows where the mean shear generates the energy required to fluidise the particles (Jenkins & Richman 1985; Sela & Goldhirsch 1998; Sela *et al.* 1996; Kumaran 2004; Kumaran 2006*a*).

https://doi.org/10.1017/jfm.2014.412 Published online by Cambridge University Press

The two widely used particle models are the hard-particle model where the particles are considered to be rigid particles interacting through instantaneous collisions (Allen & Tildesley 1992; Kumaran 2009*a*,*b*), and the soft-particle model where the particle interactions are modeled using spring-dashpot models for the forces normal and tangential to the surfaces at contact (Cundall & Strack 1979; Walton 1993; Campbell 2002, 2005). Hard-particle models cannot be easily extended to very high volume fractions due to computational errors in identifying the collision sequence when the collision frequency is large, but volume fractions as large as 0.56 have been achieved (Kumaran 2009*a*,*b*). Since there are no time scales associated with particle interactions by construction, the stresses in the hard-particle model satisfy the Bagnold law, which states that the stress is proportional to the square of the strain rate. The soft-particle models are computationally more tractable in the dense limit, because the particle interaction time is finite and it is possible to incorporate multi-body contacts. However, the computational time increases as the spring stiffness increases and the particles are made harder. The spring stiffnesses for real materials such as sand are relatively large (Cole & Peters 2007, 2008), and the spring stiffness in simulations is usually set to much lower values, because it is difficult to simulate spring stiffnesses appropriate for such materials using present computational resources (Reddy & Kumaran 2010). Surprisingly, there is now compelling evidence (Reddy & Kumaran 2007, 2010; Campbell 2011) that the time scale associated with particle interactions does not have an effect on the rheology in soft-particle simulations; the Bagnold law remains applicable and there is very little variation in the Bagnold coefficients when the spring stiffness increases by orders of magnitude, and the system transitions from a multi-body to a binary contact regime.

An important issue is the transition from a static to a flowing state. For an elastic hard sphere fluid at equilibrium with a random arrangement of particles, the maximum volume fraction is the RCP volume fraction of approximately 0.64 (Torquato 1995; Kumar & Kumaran 2005). Soft sphere packings can, of course, exceed this volume fraction, but the pressure does show a sharp increase as the RCP volume fraction is approached. It should be noted that for homogeneous shear flows of inelastic particles, the granular temperature depends on the strain rate through the energy balance equation. Here, the term 'temperature' always implies the granular temperature, which is the mean square of the particle fluctuating velocities. Hard-particle simulations (Kumaran 2009*a*,*b*) indicate that the volume fraction for 'dynamical arrest' ϕ_{ad}, where the stress diverges at constant strain rate (or the strain rate decreases to zero at constant stress) decreases as the inelasticity is increased, and asymptotes at a value of approximately $\phi_{ad} = 0.59$ for highly inelastic particles. This is consistent with the observation of a maximum volume fraction of approximately 0.59 for the flow down an inclined plane with a rough base at the bottom and a free surface on top (Silbert *et al.* 2001). This also corresponds to the shear 'dilatancy' effect, where a particle assembly with the RCP volume fraction has to expand in order to flow when sheared.

In soft-particle simulations, it has been reported that RCP volume fraction ϕ_c under shear for frictionless inelastic particles is not different from that in an elastic sphere system at equilibrium (Peyneau & Roux 2008; Chialvo, Sun & Sundaresan 2012). A part of the discrepancy may be due to the definition of the term 'frictionless': in soft-particle simulations, particle rotation and tangential stresses are usually not considered in frictionless particles, whereas in hard-particle simulations, particle rotation and tangential forces are incorporated using a tangential coefficient of restitution. A part of the discrepancy could be due to the method used for inferring

https://doi.org/10.1017/jfm.2014.412 Published online by Cambridge University Press

the maximum close packing volume fraction. In hard sphere systems, it is not possible to exceed the maximum volume fraction, and ϕ_c is inferred by extrapolating the collision frequency-volume fraction curve (at constant strain rate) and determining where it divergences. In soft-particle simulations the maximum close packing can be exceeded, because the particles are permitted to overlap, and different protocols are used to determine the close packing volume fraction. In the simulations of Chialvo *et al.* (2012), ϕ_c is determined by plotting the ratio of the root-mean-square pressure fluctuations and the absolute pressure versus volume fraction, and examining where this goes through a maximum. The results indicate a definite decrease in ϕ_c for frictional particles. For inelastic frictionless particles, the maximum of the scaled pressure fluctuation-volume fraction curve does show some variation with the coefficient of restitution, but not sufficient for the authors to conclude that ϕ_c is dependent on the coefficient of restitution. In the simulation of Peyneau & Roux (2008), ϕ_c is inferred by determining the volume fraction in the limit of zero strain rate at constant pressure. The limit of zero strain rate corresponds to an equilibrium hard-particle system, where the RCP volume fraction should be recovered. This is clearly different from the volume fraction for the divergence of frequency at constant strain rate in the hard sphere case; the limit of zero strain rate at constant pressure cannot be accessed in hard-particle simulations because both the pressure and shear stress are proportional to the square of the strain rate. Another source of discrepancy may be the difference between bounded shear flows, where the volume fraction is maintained a constant, and inclined plane flows where there is a free surface at the top and the material can dilate. However, further work is required to resolve the difference between the results of hard- and soft-particle simulations.

The standard procedure for extending kinetic theory to dense gases is to start with the Enskog equation, where the pair distribution function is introduced as a prefactor in the collision integral to incorporate the excluded volume and shadowing effects. Although dense gas theories would not intuitively be expected to be applicable to dense granular flows for multiple reasons, it appears that the theory has wider applicability than expected for sheared granular flows.

(*a*) In hard-particle systems at equilibrium, the random state of the system transitions to a crystalline state at a volume fraction of 0.49 in three dimensions; most granular flows have a volume fraction greater than 0.5, and so it was not considered possible to use theories developed for the random particle configurations. However, both hard-particle simulations of homogeneous shear at high volume fractions (Kumaran 2009*a*), as well as soft-particle simulations of the flow down an inclined plane (Silbert *et al.* 2001), show that the crystallisation transition does not take place in the presence of shear, and the system continues to be in a random state.

(*b*) It was commonly assumed that there are multi-body frictional contacts in a dense granular flow, which preclude the application of dense gas theory since the latter assumes binary instantaneous collisions. However, the binary or multi-body contact regime depends both on the volume fraction and the spring stiffness. The coordination number (number of particles in simultaneous contact with a test particle) decreases as the spring stiffness increases, due to a decrease in the duration of contact. The spring stiffnesses corresponding to real materials such as sand and glass (Cole & Peters 2007, 2008) are sufficiently large in simulations of flow down an inclined plane, so that the coordination number (number of particles in simultaneous contact with a test particle) could be smaller than one even at low angles of inclination close to onset of flow (Reddy & Kumaran 2010).

https://doi.org/10.1017/jfm.2014.412 Published online by Cambridge University Press

In addition, as noted above, there is evidence that the Bagnold law and the Bagnold coefficients in the constitutive relation do not vary as the spring stiffness decreases and the system transitions from a binary to a multi-body contact regime (Reddy & Kumaran 2010; Campbell 2011).

(*c*) For a dense granular flow down an inclined plane, the Enskog expressions for the transport coefficients, along with the pair distribution function for an elastic hard-sphere fluid near RCP, make some quantitatively and even qualitatively wrong predictions (Louge & Keast 2001; Louge 2003; Kumaran 2006*a*). They predict, for example, that as the angle of inclination increases, the volume fraction increases and the material compacts. This has cast doubts on the viability of dense gas theories for dense granular flows. However, detailed calculations of the constitutive relations up to Burnett order have shown that qualitative trends can be captured when normal stress differences are incorporated in the rheological model using expansions up to Burnett order (including second order in the gradients and terms that are quadratic in the strain rate) for the constitutive relations (Kumaran 2006*a*,*b*). However, quantitative differences persist.

(*d*) Particle correlations have been identified as the cause of the discrepancy between theory and simulations; these are not captured in the Enskog theory due to the assumption of molecular chaos. Several different types of particle correlations have been postulated, such as long range correlations (Ertas & Halsey 2002), particle clusters, angular velocity correlations among neighbouring particles (Halsey 2009), energy propagation by sound waves (Louge 2012), and a reduction in the energy dissipation rate due to particle correlations (Jenkins 2006, 2007). Simulations have not produced any conclusive evidence for the existence of these correlations in inclined plane flows in the hard-particle limit (Baran *et al.* 2006; Kumaran 2009*a*,*b*). In fact, theory (Kumaran 2006*c*, 2009*c*,*d*), simulations (Kumaran 2009*a*) and even experiments (Orpe *et al.* 2008) show that the time correlations in a sheared inelastic fluid decay much faster than that in an elastic fluid at equilibrium. A significant correlation that has been observed is the correlation in the relative velocities of neighbouring particles (Kumaran 2009*b*); the mean square of the relative velocity distribution is much smaller than that predicted by the molecular chaos approximation. This is significant because momentum and energy transport takes place primarily due to particle interactions in a dense flow. When the correlations in the relative velocity distribution are incorporated in the Enskog expansion, quantitatively accurate results are obtained (Kumaran 2009*b*).

A widely studied dense granular flow is the flow down an inclined plane with an upper free surface. Particle simulations (Silbert *et al.* 2001; Reddy & Kumaran 2010) reveal some very interesting features of this flow. At steady state, the volume fraction is nearly a constant independent of height, and the velocity profile is in agreement with that predicted by the Bagnold law in the bulk of the flow, though it does deviate from the Bagnold law in regions of thickness 3–5 particle diameters at the top and bottom. The overburden is supported not due to increase in volume fraction with depth, but because the granular temperature increases with depth. A salient feature reported in earlier studies (Pouliquen 1999; Silbert *et al.* 2001) was the dependence of the angle of h_{stop}, the residual height remaining on the inclined plane after flow, on the angle of inclination. A correlation was reported between the Froude number and (h/h_{stop}), indicating that h_{stop} may be indicative of a correlation length within the flow. However, later studies (Maheshwari & Kumaran 2012; Weinhart *et al.* 2012) reported

https://doi.org/10.1017/jfm.2014.412 Published online by Cambridge University Press

that h_{stop} also depends on base roughness, and h_{stop} could decrease to zero if the base is made energetic.

Depth-averaged models have been widely studied for shallow granular flows, specifically for avalanche flows (Savage & Hutter 1989, 1991; Gray, Wieland & Hutter 1999). In these models, it is assumed that the flow depth is small compared with the characteristic stream-wise length scale in the flow, and the velocity profile is assumed to be approximately a constant independent of depth. The flow is considered to be incompressible and volume preserving, and a Coulomb-type sliding friction law is used at the base of the avalanche. Moreover, a Mohr–Coulomb friction law is usually used for the internal stresses as well. Depth-averaged models have also been used to study heap formation by the pouring of particles (Khakhar *et al.* 2001) and in the surface flowing layer in rotating drums (Orpe & Khakhar 2007). In the depth-averaged models, equations are written for the average velocity in the cross-stream direction, and an effective depth-averaged friction condition is usually used in the momentum equation. The velocity and stress profiles in the cross-stream direction are not resolved. The purpose of the present analysis is to provide a framework for calculating the velocity and stress variations across the granular layer for shallow flows.

The velocity profiles for dense granular flows have been solved for steady and fully developed flows, where the stream-wise velocity varies only in the cross-stream direction. Numerical solutions have been obtained using continuum mass, momentum and energy equations that are inspired by dense gas theories which include correlations (Jenkins 2007; Louge 2003; Berzi & Jenkins 2011), as well as using asymptotic techniques (Kumaran 2008) where there is a systematic expansion in a small parameter. In Louge (2003), the flow is divided into a basal layer, a core and a surface layer. The pressure and shear stress consist of frictional and collisional parts, whose ratio remains constant in the core, but which is set equal to zero in the surface layer. The profile in the basal layer is determined from and angular momentum balance, and the solutions in the three layers are patched together. In Berzi & Jenkins (2011), the flow is again divided into a dilute, diffuse region at the top and a dense, algebraic region below, between which there is a sharp transition. The energy balance condition reduces to an algebraic balance between the source and dissipation in the dense algebraic region, the pressure increases linearly with height in this region due to the overburden, while the shear stress balance (presumably averaged across the width) has a contribution due to the sidewall friction. The energy balance contains the source due to mean shear and dissipation due to inelastic collisions; the latter contains a correlation length which is modeled phenomenologically. A simple linear approximation is used in the diffuse region for all variables so that the equations can be integrated using trapezoidal rule, while the algebraic balance between the rates of production and dissipation of energy is used in the dense algebraic region. The height of the flow in the diffuse and dense regions are determined from the ratio of shear stress and pressure at the boundary of the dense and diffuse region and the bottom surface. This analysis indicates that the depth of the dense region is fixed by the difference between the angle of inclination and the angle of repose, and the height of the diffuse layer depends on the coefficient of restitution.

In the asymptotic analysis (Kumaran 2008), the starting point is the mass, momentum and energy equations based on dense gas theory. The small parameter used in the asymptotic expansions is the ratio of the conduction length (obtained by a balance between the rates of conduction and dissipation of energy in the energy equation) and the total height. When the flow height is much larger than the

https://doi.org/10.1017/jfm.2014.412 Published online by Cambridge University Press

conduction length, the rate of conduction of energy can be neglected in comparison with the rates of production and dissipation. The algebraic balance between the rates of production and dissipation of energy provides a relationship between the local strain rate and the granular temperature, and the constitutive relations assume the Bagnold form. However, energy conduction is important in 'conduction layers' of thickness comparable with the conduction length at the base and the free surface. Solutions for the flow in the bulk and in the conduction layers have been derived using different approximations for the governing equations in the different regions, and asymptotic matching in between these regions region to ensure a smooth transition from one region to the other. The asymptotic solutions reproduce all of the qualitative features of the inclined plane flow, including the constant volume fraction in the bulk, the Bagnold profile, the correction to the velocity profile in the conduction layers and the variation of h_{stop} with angle of inclination for a dissipative base. It is also possible to prove an exact result, that the temperature boundary layer exists only if the volume fraction decreases as the angle of inclination increases.

Recently, a novel transition (Kumaran & Maheshwari 2012; Kumaran & Bharathraj 2013) from a disordered to an ordered state due to a decrease in the base roughness has been reported in simulations. As the base roughness is decreased, the flow abruptly transitions from a low volume fraction disordered state to a high volume fraction layered and ordered state, where hexagonally close packed layers of particles slide over each other. The Bagnold law is found to be valid in both states, but the Bagnold coefficients in the ordered state are smaller, by more than an order of magnitude, in comparison with the disordered state. The flow properties in both the ordered and disordered state are independent of the angle of inclination, the base roughness and the flow height, and the base roughness at transition shows no variation with angle of inclination and very little variation with flow height. There is shear throughout the height during the development of the disordered flow. In contrast, there is a plug at the top supported by a shearing layer at the base during the development of the ordered flow. The height of the shear layer expands linearly in time until the height becomes equal to the layer height, after which the velocity further increases to reach a steady state. This transition could provide some insight into the difference between the homogeneous shearing in the flow over rough bases, and the basal shear layer supporting a plug in the flow over flat frictional bases. Hitherto, all studies have considered only the disordered state, and further study is required for the ordered flow.

While detailed theories can be developed for a simple steady fully developed flow, it is necessary to have a macroscopic rheological model for more complicated flows. The Bagnold law has a simple form for linear shear flows, but it cannot be directly extended to more complicated deformations without a more microscopic theory. Granular dense gas theory does provide macroscopic constitutive relations. The disadvantage with dense gas theory is the relatively large number of volume-fraction-dependent material functions including the pressure, viscosity, conductivity and dissipation function. There is uncertainty about the exact form of these functions, especially in the dense regime and under flow, and small changes in the forms of these functions could have a relatively large effect on the flow characteristics. An example of this sensitivity, discussed above, is the volume fraction dependence of the angle of inclination, which changes from a decreasing to an increasing function with the inclusion of the Burnett terms in the constitutive relation. A much simpler phenomenological relation is the $\mu(I)$ model (GDR MiDi 2004), where the $\mu = (\boldsymbol{\sigma}/p)$, is related to the I parameter which is $(d\dot{\gamma}/\sqrt{p/\rho})$, where $\boldsymbol{\sigma}$ and p are the shear stress and pressure, ρ is the density and d is the particle diameter. In this case, there

https://doi.org/10.1017/jfm.2014.412 Published online by Cambridge University Press

is only one fitted function, μ, which is a function of volume fraction. This model has proved useful for a range of different flow geometries, and it has even been applied to non-viscometric flows assuming that the deviatoric parts of the stress and rate of deformation tensor are co-linear (Jop, Forterre & Pouliquen 2006; Lagree, Staron & Popinet 2011). However, the $\mu(I)$ model also has its drawbacks. Here, the prediction is for the ratio of shear stress and pressure, whereas a rheological model such as the Bagnold law should predict all components of the stress as functions of the rate of deformation tensor. In addition, the $\mu(I)$ model provides only one relation between the shear stress, pressure and the strain rate, and so an additional relation is required to determine the pressure and shear stress as a function of the strain rate. In simple flows where the pressure is prescribed, this third relation is redundant. In more complicated flows, the system of equations is usually closed by assuming that the flow is incompressible, so the pressure assumes the value necessary to satisfy incompressibility. In the present analysis, we provide some further insight into conditions under which flows can be considered incompressible.

Here, we propose simplified equations for 'shallow dense granular flows', dense because the volume fraction is close to that for dynamical arrest, and shallow because the flow is nearly unidirectional and the cross-stream layer height h is small compared to the stream-wise characteristic flow length L. In the shallow limit, the equations are simplified by neglecting terms of $O(h/L)$ or smaller, using methods similar to boundary layer theories (Schlichting & Gersten 2000). The description of shallow flows is also simplified because the largest component of the rate of deformation tensor is the cross-stream derivative of the stream-wise velocity. For a hard-particle fluid in the dense limit, the pressure and transport coefficients increase proportional to the collision frequency or the 'pair distribution function' in the Enskog theory. Simulations (Kumaran 2009*a*,*b*) have shown that the pair distribution function diverges proportional to $(\phi_{ad}-\phi)^{-\alpha}$ in the dense limit, where α is a positive exponent. While α is 1 for elastic hard spheres (Torquato 1995), different simulations predict different values of α for inelastic hard sphere systems. Here we do not assume a specific value for α, but only utilise the power law divergence which seems universal. A 'dense' system is defined as one where the volume fraction is close to ϕ_{ad} and the pair distribution function is numerically large. In this case, the derivative of the pair distribution function with volume fraction is larger than the pair distribution function itself, $(\mathrm{d}\chi/\mathrm{d}\phi) \gg (\chi/\phi)$, where χ is the pair distribution function at contact. There are two small parameters in the analysis, the 'shallow' parameter which is the ratio of length scales (h/L) and the 'dense' parameter $\chi/(\phi(\mathrm{d}\chi/\mathrm{d}\phi))$. The expansion in (h/L) is standard in boundary layer theories, and so it is not considered here, but the expansion in parameter $\chi/(\phi(\mathrm{d}\chi/\mathrm{d}\phi))$ is non-standard. The mass conservation equation reduces to the incompressible form (divergence of velocity is zero) in the leading approximation, and the constitutive relations for the shear and normal stress reduce to the Bagnold relations. Compressibility effects provide the first corrections to the velocity fields. Here, a systematic method for correcting the incompressible equations to include the effect of compressibility is derived.

The equations are applied to two configurations, the flow development from a plug flow to a fully developed Bagnold profile, and the development of the boundary layer at the base when there is an abrupt transition from a smooth base with a slip condition to a rough base with a no-slip condition, as shown in figure 1. A separation-of-variables procedure is used in the developing flow analysis, where the departure from the Bagnold profile is expressed as the product of an exponentially decaying function in the stream-wise x coordinate, and an eigenfunction solution

https://doi.org/10.1017/jfm.2014.412 Published online by Cambridge University Press

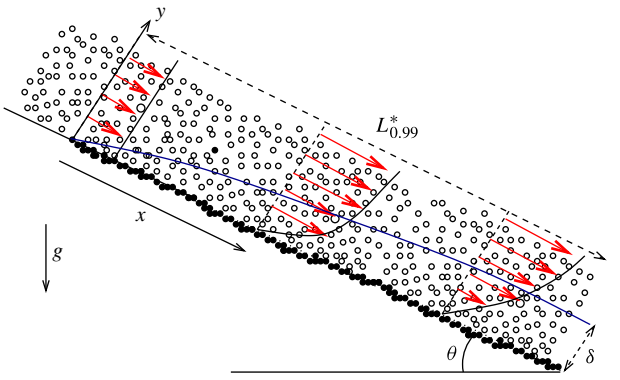


FIGURE 1. (Colour online) Configuration and coordinate system for analysing the developing flow down an inclined plane from a plug flow to a fully developed Bagnold profile.

in the cross-stream y coordinate. A linearisation approximation is used, and so the solution is valid only at downstream locations where the departure from the Bagnold profile is small. At upstream locations near the start of the rough section of the base, the momentum disturbance is restricted to a 'boundary layer' of thickness small compared with the layer height. Here, a boundary layer analysis, similar to the Falkner–Skan analysis (Schlichting & Gersten 2000), is used to determine the velocity profile. In the boundary layer analysis, a general form for the variation of the stream-wise velocity, $U(x)$, is considered.

Important parameters in the analysis are the flow development length L for the developing flow, and a length scale l for the boundary layer thickness. These length scales are related to the Bagnold coefficients and their derivatives with respect to volume fraction. These can be derived from kinetic theories, but such a derivation is not used here because of uncertainty in the exact form of the constitutive relations when there are correlations. Here, it is shown that both these length scales can be determined from simulations of the unsteady fully developed flow down an inclined plane, using the characteristic time scale τ for flow development (Kumaran & Bharathraj 2013). This enables the quantitative prediction of the length scale for flow development and the boundary layer thickness. The flow development length is independent of the flow velocity or angle of inclination, and it increases proportional to h^3. The length scale l is independent of the height and velocity of the flowing layer, and depends only on the Bagnold coefficients and their derivatives, and the density of the flow. It is also possible to define the Reynolds number Re, which is the ratio of the inertial terms and the divergence of the stress in the momentum conservation equations, and the compressibility number (Co), which is the ratio of the volume fraction variation and the average volume fraction. The Reynolds number turns out to be independent of velocity, because both the inertial terms and the Bagnold stress are proportional to the square of the velocity, and it is equal to $(h/d)^2$ times a function of the Bagnold coefficients, where d is the particle diameter. The compressibility number is proportional to $\chi/(\phi(\mathrm{d}\chi/\mathrm{d}\phi))$.

The governing equations and the general constitutive relation used in the analysis are provided in the next section. The equations are simplified using the limits $(h/L) \ll 1$ and $\chi/(\phi(\mathrm{d}\chi/\mathrm{d}\phi)) \ll 1$ to derive the dense shallow flow equations in § 3. The late stage flow development is analysed using separation of variables in § 4, and

https://doi.org/10.1017/jfm.2014.412 Published online by Cambridge University Press

the boundary layer equations are solved using a similarity solution in § 5. In § 6, the important conclusions are summarised, and numerical estimates are determined for the flow development length, boundary layer thickness, and the Reynolds and compressibility number in § 7.

2. Governing equations

In order to simplify the governing equations, the mass of the particles is set equal to 1, so that the equations do not contain the mass dimension. The mass, momentum and energy conservation equations for the granular flow are

$$\frac{\partial \rho}{\partial t} + \boldsymbol{\nabla} \cdot (\rho \boldsymbol{u}) = 0, \tag{2.1}$$

$$\rho \left(\frac{\partial \boldsymbol{u}}{\partial t} + \boldsymbol{u} \cdot \boldsymbol{\nabla} \boldsymbol{u} \right) = \boldsymbol{\nabla} \cdot \boldsymbol{\sigma} + \rho \boldsymbol{g}, \tag{2.2}$$

$$\rho C_v \left(\frac{\partial T}{\partial t} + \boldsymbol{u} \cdot \boldsymbol{\nabla} T \right) = \boldsymbol{\sigma} : \boldsymbol{\nabla} \boldsymbol{u} - D + \boldsymbol{\nabla} \cdot (K \boldsymbol{\nabla} T), \tag{2.3}$$

where ρ and $\boldsymbol{u}$ are the density and velocity fields, T is the granular temperature with dimension $\mathscr{L}^2 \mathscr{T}^{-2}$, C_v is the specific heat at constant volume which is (3/2) for particles with translation degrees of freedom and 3 for particles with both translational and rotational degrees of freedom, $\boldsymbol{\sigma}$ is the stress tensor with dimension $\mathscr{L}^{-1} \mathscr{T}^{-2}$, $\boldsymbol{g}$ is the acceleration due to gravity and D is the rate of energy dissipation per unit volume with dimensions $\mathscr{L}^{-1} \mathscr{T}^{-3}$. Here, $\mathscr{L}$ and $\mathscr{T}$ are the length and time dimensions, respectively. Note that the density is defined as the number of particles per unit volume, since the particle mass is set equal to 1.

In order to write the stress tensor in a frame-invariant form, the local strain rate tensor, g_{ij}, is separated into the isotropic ($\delta_{ij} g_{kk}$), symmetric traceless (e_{ij}) and antisymmetric (a_{ij}) components,

$$g_{ij} = e_{ij} + a_{ij} + \delta_{ij} g_{kk}, \tag{2.4}$$

where δ_{ij} is the identity tensor, and indicial notation is used to represent the components of vectors and tensors. The most general form for the symmetric stress tensor, up to quadratic order in the rate of deformation tensor, can be written as

$$\begin{aligned} \sigma_{ij} \;=\; & -p\delta_{ij} + 2\mu e_{ij} + \zeta \delta_{ij} g_{kk} + B_{EE}(e_{ik}e_{kj} - (\delta_{ij}/3)e_{kl}e_{lk}) \\ & + B'_{EE}\delta_{ij}e_{kl}e_{lk} + B_{EA}(e_{ik}a_{kj} - a_{ik}e_{kj}) \\ & + B_{AA}(a_{ik}a_{kj} - (\delta_{ij}/3)a_{kl}a_{lk}) + B'_{AA}\delta_{ij}a_{kl}a_{lk} \\ & + B_{EG}e_{ij}g_{kk} + B_{GG}\delta_{ij}g_{kk}g_{ll}, \end{aligned} \tag{2.5}$$

where p is the isotropic pressure, μ and ζ are the viscosity and bulk viscosity coefficients and $B_{EE} - B_{GG}$ are the Burnett coefficients. The stress σ_{ij} in (2.5) has been defined as the force per area in the i direction acting at a surface with outward unit normal in the j direction. It should be noted that the viscosity coefficients and the pressure depend on the temperature, which is related to the strain rate through energy balance.

A simplified form of the stress tensor is used in the present analysis of a developing dense granular flow. The simplifications result from the two-dimensional and nearly unidirectional nature of the flow, and the consideration that the stream-wise length

https://doi.org/10.1017/jfm.2014.412 Published online by Cambridge University Press

scale for flow development L (in the x direction) is much larger than the flow height h. In this case, the largest term in the rate of deformation tensor is $(\partial u_x/\partial y)\boldsymbol{e}_x\boldsymbol{e}_y$, where $\boldsymbol{e}_x$ and $\boldsymbol{e}_y$ are the unit vectors in the stream-wise and cross-stream directions, respectively. The cross-stream velocity scales as $u_y \sim (u_x h/L)$ from mass conservation. The largest terms in the equation for the stress are then given by

$$\sigma_{xx} = \sigma_{yy} = -p + B\left(\frac{\partial u_x}{\partial y}\right)^2, \tag{2.6}$$

$$\sigma_{xy} = \mu\frac{\partial u_x}{\partial y}, \tag{2.7}$$

where $B = (B_{EE}/12 + B'_{EE}/2)$ is a Burnett coefficient. Based on dimensional analysis, the pressure, viscosity, Burnett coefficient, the thermal conductivity and the dissipation rate in the energy equation for hard particles are expressed in two ways, the first of which is exact and the second is an approximation in the dense limit:

$$p = (p_\phi T/d^3) \sim (p_c \chi T/d^3), \tag{2.8}$$

$$\mu = (\mu_\phi T^{1/2}/d^2) \sim (\mu_c \chi T^{1/2}/d^2), \tag{2.9}$$

$$B = (B_\phi/d) \sim (B_c \chi/d), \tag{2.10}$$

$$K = (K_\phi T^{1/2}/d^2) \sim (K_c \chi T^{1/2}/d^2), \tag{2.11}$$

$$D = (D_\phi/d^4)T^{3/2} \sim (D_c \chi/d^4)T^{3/2}. \tag{2.12}$$

Here p_ϕ, μ_ϕ, B_ϕ K_ϕ and D_ϕ are dimensionless functions of the volume fraction, while p_c, μ_c, B_c, K_c and D_c are constants, and χ is the dimensionless pair distribution function in the Enskog equation which is numerically large in the dense limit.

3. Equations of motion

The two-dimensional equations of motion at steady state are

$$\frac{\partial(\rho u_x)}{\partial x} + \frac{\partial(\rho u_y)}{\partial y} = 0, \tag{3.1}$$

$$\rho\left(u_x\frac{\partial u_x}{\partial x} + u_y\frac{\partial u_x}{\partial y}\right) = \frac{\partial \sigma_{xx}}{\partial x} + \frac{\partial \sigma_{xy}}{\partial y} + \rho g_x, \tag{3.2}$$

$$\rho\left(u_x\frac{\partial u_y}{\partial x} + u_y\frac{\partial u_y}{\partial y}\right) = \frac{\partial \sigma_{xy}}{\partial x} + \frac{\partial \sigma_{yy}}{\partial y} + \rho g_y, \tag{3.3}$$

$$\rho C_v\left(u_x\frac{\partial T}{\partial x} + u_y\frac{\partial T}{\partial y}\right) = \sigma_{xx}\frac{\partial u_x}{\partial x} + \sigma_{xy}\left(\frac{\partial u_x}{\partial y} + \frac{\partial u_y}{\partial x}\right) + \sigma_{yy}\frac{\partial u_y}{\partial y} - D + \frac{\partial}{\partial x}\left(K\frac{\partial T}{\partial x}\right) + \frac{\partial}{\partial y}\left(K\frac{\partial T}{\partial y}\right). \tag{3.4}$$

The scaled coordinates are defined as $x^* = (x/L)$ and $y^* = (y/h)$, where the stream-wise length scale L is considered to be large compared with the flow height h. The conditions for the validity of the assumption $L \gg h$ are discussed a little later. The stream-wise velocity is scaled by the product of the characteristic strain rate $\dot{\gamma}$ and the height h, $u_x^* = (u_x/\dot{\gamma}h)$. The cross-stream velocity u_y scales as (hu_x/L) from the mass conservation equation, and so we define the scaled cross-stream velocity

https://doi.org/10.1017/jfm.2014.412 Published online by Cambridge University Press

as $u_y^* = (u_y/(\dot{\gamma}h^2/L))$. The spatial derivatives of the density are expressed in terms of the spatial derivatives of the pair distribution function,

$$\frac{\partial \rho}{\partial x_i} = \frac{1}{\chi_\rho}\frac{\partial \chi}{\partial x_i}, \tag{3.5}$$

where

$$\chi_\rho = \frac{\partial \chi}{\partial \rho}. \tag{3.6}$$

To estimate the relative magnitudes of the different terms in the conservation equations, we define the scaled density $\rho^* = (\rho/\bar{\rho})$, the scaled pair distribution function and its derivative as $\chi^* = (\chi/\Xi)$ and $\chi_\rho^* = (\chi_\rho/\Xi_\rho)$, where $\bar{\rho}$, Ξ and Ξ_ρ are mean density, the scales for the pair distribution function and its derivative, which can be considered as the maximum values in the domain. The maximum values of ρ^*, χ^* and χ_ρ^* are then equal to 1. The temperature is expressed as $T = \Upsilon T^*$, where Υ, the scale for the temperature variations, is related to the strain rate through the energy equation, and T^*, the scaled temperature, is $O(1)$. The scaled mass and momentum equations can be simplified by neglecting the stream-wise derivatives on the right-hand sides, since these are small compared with the cross-stream derivatives for $h \ll L$. The simplified equations are

$$\frac{\partial u_x^*}{\partial x^*} + \frac{\partial u_y^*}{\partial y^*} + \frac{\Xi}{\bar{\rho}\Xi_\rho}\frac{1}{\rho^*}\left(u_x^*\frac{\partial \chi^*}{\partial x^*} + u_y^*\frac{\partial \chi^*}{\partial y^*}\right) = 0, \tag{3.7}$$

$$\frac{\bar{\rho}\dot{\gamma}^2h^2}{L}\rho^*\left(u_x^*\frac{\partial u_x^*}{\partial x^*} + u_y^*\frac{\partial u_x^*}{\partial y^*}\right) = \frac{\mu_c \Xi \Upsilon^{1/2}\dot{\gamma}}{d^2h}\frac{\partial}{\partial y^*}\left(T^{*1/2}\frac{\partial u_x^*}{\partial y^*}\right) + \bar{\rho}\rho^* g_x, \tag{3.8}$$

$$\begin{aligned}\frac{\bar{\rho}\dot{\gamma}^2h^3}{L^2}\rho^*&\left(u_x^*\frac{\partial u_y^*}{\partial x^*} + u_y^*\frac{\partial u_y^*}{\partial y^*}\right)\\ &= -\frac{p_c\Xi\Upsilon}{d^3h}\frac{\partial(\chi^*T^*)}{\partial y^*} + \frac{B_c\Xi\dot{\gamma}^2}{dh}\frac{\partial}{\partial y^*}\left(\left(\frac{\partial u_x^*}{\partial y^*}\right)^2\right) + \bar{\rho}\rho^* g_y,\end{aligned} \tag{3.9}$$

$$\begin{aligned}\frac{\bar{\rho}C_v\dot{\gamma}h\Upsilon}{L}\rho^*&\left(u_x^*\frac{\partial T^*}{\partial x^*} + u_y^*\frac{\partial T^*}{\partial y^*}\right)\\ &= \frac{\mu_c\Xi\Upsilon^{1/2}\dot{\gamma}^2}{d^2}T^{*1/2}\left(\frac{\partial u_x^*}{\partial y^*}\right)^2 - \frac{D_c\Xi\Upsilon^{3/2}}{d^4}\chi^*T^{*3/2}\\ &\quad + \frac{K_c\Xi\Upsilon^{3/2}}{d^2h^2}\frac{\partial}{\partial y^*}\left(\chi^*T^{*1/2}\frac{\partial T^*}{\partial y^*}\right).\end{aligned} \tag{3.10}$$

The following further approximations can be made.

(*a*) In the mass conservation equation, the ratio $(\Xi/\rho\Xi_\rho)$ can be written as $(\Xi/\phi\Xi_\phi)$, where Ξ_ϕ is the maximum value of $(\partial\chi/\partial\phi)$ in the domain. In the dense limit $(\phi_{ad} - \phi) \ll 1$, the pair distribution function diverges as $(\phi_{ad} - \phi)^{-\alpha}$, where ϕ is the volume fraction and ϕ_{ad} is the volume fraction for arrested dynamics. The ratio $(\Xi/\phi\Xi_\phi) \sim (\phi_{ad} - \phi)$ for $\phi_{ad} - \phi \ll 1$. In this case, the second term on the right-hand side of (3.7) is small compared with the first term, and the flow can be considered effectively incompressible. The error made due to the incompressibility assumption is $O(\phi_{ad} - \phi)$.

(*b*) It is clear that the rate of conduction of energy in the energy balance equation is $O(d^2/h^2)$ smaller than the rate of dissipation, and so the rate of conduction of energy can be neglected for $(d/h) \ll 1$.

https://doi.org/10.1017/jfm.2014.412 Published online by Cambridge University Press

(*c*) A balance between the rates of production and dissipation of energy, the first and second terms on the right-hand side of the energy balance equation (3.10), provides $\Upsilon \sim (\dot{\gamma} d)^2$. This is useful for evaluating the magnitudes of the terms on the left- and right-hand sides of the momentum equations (3.8) and (3.9).

(*d*) A balance between the gravitational force and the leading order contribution to the divergence of the stress, in (3.9), indicates that $\Upsilon \sim ((\bar{\rho} d^3)(g_y h)/\Xi)$. For a dense flow, $\bar{\rho} d^3 \sim 1$, and so the granular temperature scales as $(g_y h/\Xi)$ for a dense flow, and $\dot{\gamma} \sim \sqrt{g_y h/\Xi d^2}$.

(*e*) The ratio of the convective term on the left of (3.8), and the largest contribution to the divergence of the stress, the first term on the right-hand side of (3.8), is $((\bar{\rho} d^3/\Xi)(h/L)(h^2/d^2))$.
For a dense flow with $\Xi \gg 1$ and $(h/d) \gg 1$, this ratio depends on the relative magnitude of Ξ and $(h/d)^2$. Here, we consider the limit where $(h^2/d^2/\Xi) \gg 1$; the validity of this approximation is discussed in § 7. In this case, the length scale L for the flow development scales as $(h^3/d^2\Xi)$, so that the convective terms on the left-hand side of (3.8) are comparable with the largest contribution to the stress divergence on the right-hand side. It should be noted that the flow development length L increases proportional to h^3. The shallow flow approximation is valid for $L \gg h$, or $(h^2/d^2\Xi) \gg 1$.

(*f*) The ratio of the convective term on the left-hand side of the y momentum equation (3.9) and the largest contribution to the divergence of the stress on the right-hand side is $((\bar{\rho} d^3/\Xi)(h/d)^2(h/L)^2)$. Using the estimate $L \sim (h^2/d^2\Xi)$ and $\bar{\rho} d^3 \sim 1$, the convective terms on the left-hand side are $O(h/L)$ smaller than the terms on the right.

(*g*) The ratio of the rate of convection of energy on the left-hand side of (3.10) and the rate of dissipation of energy is $(\bar{\rho} C_v \dot{\gamma} h d^4/\Xi L \Upsilon^{1/2}) \sim ((\bar{\rho} d^3) C_v (\dot{\gamma} d/\Upsilon^{1/2})(h/L\Xi))$. Since $(\bar{\rho} d^3)$, C_v and $(\dot{\gamma} d/\Upsilon^{1/2})$ are $O(1)$, this ratio is proportional to $(h/L\Xi)$. Using the estimate $L \sim (h^3/d^2\Xi)$, the ratio of the energy convection and dissipation is $O(d^2/h^2)$.

From the above discussion, if we neglect terms of $O(h/L)$, $O(d^2/h^2)$ and $O(\Xi/\bar{\rho}\Xi_\rho)$, the energy balance equation reduces to an algebraic equation,

$$\frac{\mu_\phi T^{1/2}}{d^2}\left(\frac{\partial u_x}{\partial y}\right)^2 - \frac{D_\phi T^{3/2}}{d^4} = 0. \tag{3.11}$$

This can be solved to obtain an expression for the temperature in terms of the local strain rate,

$$T = \frac{\mu_\phi d^2}{D_\phi}\left(\frac{\partial u_x}{\partial y}\right)^2. \tag{3.12}$$

This is inserted into the mass and momentum conservation equations, and terms of $O(h/L)$ are neglected, to obtain

$$\frac{\partial u_x}{\partial x} + \frac{\partial u_y}{\partial y} = 0, \tag{3.13}$$

$$\rho\left(u_x\frac{\partial u_x}{\partial x} + u_y\frac{\partial u_x}{\partial y}\right) = \frac{\partial}{\partial y}\left(B_{xy}(\phi)\left(\frac{\partial u_x}{\partial y}\right)\left|\frac{\partial u_x}{\partial y}\right|\right) + \rho g_x, \tag{3.14}$$

$$0 = -\frac{\partial}{\partial y}\left(B_{yy}(\phi)\left(\frac{\partial u_x}{\partial y}\right)\left|\frac{\partial u_x}{\partial y}\right|\right) + \rho g_y, \tag{3.15}$$

https://doi.org/10.1017/jfm.2014.412 Published online by Cambridge University Press

where the Bagnold coefficients are $B_{xy} = (\mu_\phi^{3/2}/D_\phi^{1/2}d)$ and $B_{yy} = ((\ p_\phi\mu_\phi/D_\phi d) - (B_\phi/d))$. In the remainder of the analysis, we consider u_x to be positive and an increasing function of y, except where explicitly stated, and so we set $|\partial u_x/\partial y| = (\partial u_x/\partial y)$.

From point (e) above, it is clear that the largest terms neglected in the momentum and energy equations are $O(h/L)$, while the largest term neglected in the mass conservation equation is $O(\Xi/\bar{\rho}\Xi_\rho)$. Therefore, the largest correction to the conservation equations depend on which of these two contributions is larger.

(a) For $(\Xi/\bar{\rho}\Xi_\rho) \ll (h/L)$, the largest correction is $O(h/L)$ due to non-parallel effects. The algebraic relation between the temperature and strain rate (3.12) is still valid, but the convective terms on the left-hand side of the y momentum equation (3.9) have to be included. This can be done by a standard regular perturbation procedure in boundary layer theory, and so we do not pursue this further.

(b) For $(\Xi/\bar{\rho}\Xi_\rho) \gg (h/L)$, the compressibility effects in the mass conservation equation provide the largest correction to the boundary layer equations. In this case, the mass conservation equation has to be modified to include compressibility effects,

$$\phi\left(\frac{\partial u_x}{\partial x} + \frac{\partial u_y}{\partial y}\right) + u_x\frac{\partial \phi}{\partial x} + u_y\frac{\partial \phi}{\partial y} = 0, \tag{3.16}$$

while the momentum conservation equations (3.14) and (3.15) and the algebraic relation between temperature and strain rate (3.12) remain unchanged. In (3.16), it is more convenient to use the volume fraction instead of the density, since the pair distribution function and the Bagnold coefficients are usually expressed in terms of the volume fraction.

In the incompressible limit, it is convenient to express the velocity in terms of the stream function ψ, so that the incompressibility condition is satisfied,

$$u_x = \frac{\partial \psi}{\partial y}, \tag{3.17}$$

$$u_y = -\frac{\partial \psi}{\partial x}. \tag{3.18}$$

An expansion up to linear order in the volume fraction is used for the Bagnold coefficients,

$$B_{ij}(\phi) = \bar{B}_{ij} + \bar{B}_{\phi ij}\phi', \tag{3.19}$$

where $\bar{B}_{ij} = B_{ij}|_{\phi=\bar{\phi}}$ and $\bar{B}_{\phi ij} = (\mathrm{d}B_{ij}/\mathrm{d}\phi)|_{\phi=\bar{\phi}}$, where $\bar{\phi}$ is a reference volume fraction. Equation (3.19) can be substituted in (3.15) to obtain ϕ' for the case where the mass density is approximately a constant,

$$\phi' = \frac{\displaystyle\int_{y_0}^{y} \mathrm{d}y'\, \rho g_y}{\bar{B}_{\phi yy}(\partial u_x/\partial y)^2} - \frac{\bar{B}_{yy}}{\bar{B}_{\phi yy}}, \tag{3.20}$$

where y_0 is a reference height where the stress is zero. Note that g_y is negative for the coordinate system defined in figure 1. The expression (3.20) is inserted into the x momentum equation (3.14) to obtain

$$u_x\frac{\partial u_x}{\partial x} + u_y\frac{\partial u_x}{\partial y} = g_x + \frac{g_y\bar{B}_{\phi xy}}{\bar{B}_{\phi yy}} + \rho^{-1}\frac{\partial}{\partial y}\left(\mathscr{B}\frac{\partial u_x}{\partial y}\left|\frac{\partial u_x}{\partial y}\right|\right), \tag{3.21}$$

https://doi.org/10.1017/jfm.2014.412 Published online by Cambridge University Press

where $\mathscr{B} = (\bar{B}_{xy} - (\bar{B}_{yy}\bar{B}_{\phi xy}/\bar{B}_{\phi yy}))$. Equation (3.18) can be used to express the velocity in terms of the stream function, to obtain a nonlinear equation for the stream function,

$$\frac{\partial \psi}{\partial y}\frac{\partial^2 \psi}{\partial x \partial y} - \frac{\partial \psi}{\partial x}\frac{\partial^2 \psi}{\partial y^2} = g_x + \frac{g_y \bar{B}_{\phi xy}}{\bar{B}_{\phi yy}} + \rho^{-1}\frac{\partial}{\partial y}\left(\mathscr{B}\frac{\partial^2 \psi}{\partial y^2}\left|\frac{\partial^2 \psi}{\partial y^2}\right|\right). \tag{3.22}$$

This is the equivalent of the boundary layer equation for the stream function for a Newtonian fluid. In the case of a compressible flow, an equation for u_x can be obtained by first expressing u_y in terms of u_x using (3.14),

$$u_y = \left(\frac{\partial u_x}{\partial y}\right)^{-1}\left[-u_x\frac{\partial u_x}{\partial x} + g_x + \frac{g_y \bar{B}_{\phi xy}}{\bar{B}_{\phi yy}} + \rho^{-1}\frac{\partial}{\partial y}\left(\mathscr{B}\frac{\partial u_x}{\partial y}\left|\frac{\partial u_x}{\partial y}\right|\right)\right]. \tag{3.23}$$

This can be inserted into the mass conservation equation, (3.13), to obtain a partial differential equation for u_x,

$$\frac{\partial u_x}{\partial x} + \frac{\partial u_y}{\partial y} + \frac{1}{\bar{\phi}}\frac{\partial}{\partial x}\left(u_x\left(\frac{\int_{y_0}^{y} \mathrm{d}y' \rho g_y}{\bar{B}_{\phi yy}(\partial u_x/\partial y)^2} - \frac{\bar{B}_{yy}}{\bar{B}_{\phi yy}}\right)\right) + \frac{\partial}{\partial y}\left(u_y\left(\frac{\int_{y_0}^{y} \mathrm{d}y' \rho g_y}{\bar{B}_{\phi yy}(\partial u_x/\partial y)^2} - \frac{\bar{B}_{yy}}{\bar{B}_{\phi yy}}\right)\right) = 0, \tag{3.24}$$

where u_y is given by (3.23). The above equation is a third-order integro-differential equation for the velocity component u_x, which is more difficult to solve than (3.22), due to the height integrals in the third and fourth terms on the left-hand side.

In the developing flow analysis in the next section, we use a simplified form of (3.22) for the velocity profile in the incompressible limit, and a linearised form of (3.24) to examine the effect of variations in volume fraction in the inertial terms in the mass and stream-wise momentum conservation equation. It should be noted that volume fraction variations are already included in the divergence of the stress on the right-hand side of (3.22), through the dependence of the Bagnold coefficients on the volume fraction. This is because small changes in volume fraction cause only small changes in the density, but cause large changes in the Bagnold coefficients for a dense and highly collisional flow. In the boundary layer analysis in § 5, (3.24) is solved using the strong assumption that the flow thickness is much larger than the height of the boundary layer. In this case, the modification of the overburden due to the density variation in the boundary layer is neglected, and the density is considered to be a constant value appropriate for the outer flow. With this approximation, (3.24) reduces to a third-order differential equation which can be solved for the velocity field in the boundary layer. It is shown that (3.24) reduces to (3.22) in the incompressible limit, although (3.24) can be systematically extended to the compressible regime.

The sign of $\mathscr{B} = (\bar{B}_{xy} - (\bar{B}_{yy}\bar{B}_{\phi xy}/\bar{B}_{\phi yy}))$ in (3.22) and (3.23) has important implications for the existence of solutions (note that all Bagnold coefficients are positive). It has been shown (Kumaran 2008) that $\mathscr{B}$ is positive if the flow has the intuitively expected property that the volume fraction decreases as the angle of inclination increases for the steady state. In the physically unrealistic case where the

https://doi.org/10.1017/jfm.2014.412 Published online by Cambridge University Press

volume fraction increases with angle of inclination, $\mathscr{B}$ is negative. There is an exact theorem which states that a temperature boundary layer exists only if the volume fraction decreases as the angle of inclination increases. It was shown in the analysis of the transient velocity profile (Kumaran & Bharathraj 2013) that the transients decay in the long time limit only if $\mathscr{B}$ is positive. The analysis of the developing flow in the next section indicates that the length scale for flow development (4.27) is positive only if the $\mathscr{B}$ is positive; otherwise, an unphysical negative value is obtained for the length. Similarly, in the boundary layer solution in § 5, the length scale l (5.6) in the expression for the boundary layer thickness is real only if $\mathscr{B}$ is positive. Thus, the positivity of $\mathscr{B}$ is a basic requirement for the existence of solutions for different types of dense shallow granular flows. Here, $\mathscr{B}$ is considered to be positive throughout the analysis.

The total height of the granular layer will, in general, change as the flow develops. The change in height is determined from the kinematic condition which, at steady state, is

$$\frac{\mathrm{D}h}{\mathrm{D}t} = u_y \quad \text{at } y = h \tag{3.25}$$

where the substantial derivative is $(\mathrm{D}/\mathrm{D}t) = (\partial/\partial t) + u_x(\partial/\partial x)$, and the boundary condition is applied at the surface $y = h$. At the free surface, the zero normal and shear stress conditions are

$$\boldsymbol{t}\cdot\boldsymbol{\sigma}\cdot\boldsymbol{n} = 0 \quad \text{at } y = h \tag{3.26}$$

$$\boldsymbol{n}\cdot\boldsymbol{\sigma}\cdot\boldsymbol{n} = 0 \quad \text{at } y = h \tag{3.27}$$

where $\boldsymbol{t}$ and $\boldsymbol{n}$ are the unit tangent and normal to the deformed surface.

The height is determined from the mass conservation condition, that the total mass flow rate across any x location is the same

$$\frac{\mathrm{d}}{\mathrm{d}x}\int_0^{h(x)} \mathrm{d}y\, \rho u_x = 0. \tag{3.28}$$

Using Leibniz rule, and expressing the density in terms of the volume fraction, the above equation can be reduced to

$$\int_0^{h(x)} \mathrm{d}y\, \frac{\partial(\phi u_x)}{\partial x} + \frac{\mathrm{d}h}{\mathrm{d}x}(\phi u_x)|_{y=h} = 0. \tag{3.29}$$

It is convenient define a scaled y coordinate, $y^* = (y/h(x))$, where $h(x)$ is the height at the stream-wise location x. The independent variables are, then, transformed from (x, y) to (x, y^*), and the derivatives are transformed as

$$\frac{\partial}{\partial x} \rightarrow \left(\frac{\partial}{\partial x} - \frac{y^*}{h}\frac{\mathrm{d}h}{\mathrm{d}x}\frac{\partial}{\partial y^*}\right) \tag{3.30}$$

$$\frac{\partial}{\partial y} \rightarrow \frac{1}{h}\frac{\partial}{\partial y^*}. \tag{3.31}$$

The (3.29) can be expressed in terms of y^*, and simplified using integration by parts, to obtain

$$\int_0^1 h\,\mathrm{d}y^*\, \frac{\partial(\phi u_x)}{\partial x} + \phi u_x|_{y^*=1}\frac{\mathrm{d}h}{\mathrm{d}x} = 0. \tag{3.32}$$

https://doi.org/10.1017/jfm.2014.412 Published online by Cambridge University Press

This provides us with an equation for the variation of the height, $(\mathrm{d}h/\mathrm{d}x)$,

$$\frac{1}{h}\frac{\mathrm{d}h}{\mathrm{d}x} = \frac{\displaystyle\int_0^1 \mathrm{d}y^* \frac{\partial(\phi u_x)}{\partial x}}{\phi u_x|_{y^*=1}}. \tag{3.33}$$

In the analysis in § 4.1, a linearisation approximation is used to treat the height variation in the developing flow. The height is considered to be of the form $h(x) = \bar{h} + h'(x)$, where $h' \ll \bar{h}$. The height perturbation is obtained by a linearisation of the kinematic condition (3.25) about the height $\bar{h}$ of the fully developed flow. In the case of the boundary layer flow in § 5, the thickness of the boundary layer is considered to be small compared with the total height. Therefore, the flow deceleration in the boundary layer will result in a correction to the height which is proportional to (δ/h), the ratio of the boundary layer thickness and the flow height. This variation is neglected in the present analysis.

The (3.14)–(3.16) differ from the Savage & Hutter (1989) model in many ways. The equations of Savage and Hutter are depth-averaged equations, where the dynamical variables are the depth-averaged velocity and stresses. In contrast, we solve for the velocity and stress profiles in the cross-stream directions in the present analysis, and so there is no assumption about the forms of the velocity profiles. In the model of Savage & Hutter (1989), the relation between the depth-averaged normal stresses in the flow and gradient directions is determined assuming the material is of the Mohr–Coulomb type, while the shear and normal stress at the base are related through a Coulomb criterion (it turns out that the depth-averaged shear stress does not appear in the final equations). In addition, the strain rate does not explicitly appear in the analysis. In contrast, the Bagnold constitutive relations are used here to relate both components of the stress to the rate of deformation tensor. In this respect, the present analysis is also different from the $\mu(I)$ model of GDR MiDi (2004) where there is one constitutive relation which relates the shear stress, pressure and the strain rate locally. Due to this, it is not possible to obtain independently the shear stress and the pressure in terms of the strain rate. Closure is achieved using the incompressibility assumption in the $\mu(I)$ model, whereby the pressure assumes the necessary value to ensure constant density everywhere in the flow. Due to this, it is difficult to use the $\mu(I)$ model in situations or regions of the flow where there is a variation in the volume fraction. In the present study, systematic method for including volume fraction variations has been derived and applied to situations for cases where the variation in the volume fraction is small compared with the average value. Even though the effect of the variation in volume fraction on the inertial terms in the conservation equations is neglected in the leading approximation, it is important to note that the leading approximation does contain the effect of volume fraction variations on the Bagnold coefficients.

4. Late stage flow development

4.1. *Incompressible limit*

In the late stages of flow evolution, the volume fraction and velocity can be expressed as the sum

$$\phi(x, y) = \bar{\phi} + \phi'(x, y) + \phi''(x, y), \tag{4.1}$$

$$u_x(x, y) = \bar{u}_x(y) + u'_x(x, y) + u''_x(x, y), \tag{4.2}$$

$$u_y(x, y) = u'_y(x, y) + u''_y(x, y), \tag{4.3}$$

https://doi.org/10.1017/jfm.2014.412 Published online by Cambridge University Press

and the height h is expanded as

$$h = \bar{h} + h'(x) + h''(x) \tag{4.4}$$

where $(\bar{\phi},\ \bar{u}_x(y),\ 0,\ \bar{h})$ are the fully developed volume fraction, velocity fields and height, and $(\phi',\ u'_x(x,\ y),\ u'_y(x,\ y),\ h'(x))$ are the developing parts of the volume fraction and velocity fields in the incompressible limit which are solutions of (3.22), while $(\phi'',\ u''_x,\ u''_y)$ are the corrections to the solution when the compressibility effects are introduced in the mass conservation equation (3.16). The developing parts, $(\phi' + \phi'',\ u'_x + u''_x,\ u'_y + u''_y,\ h' + h'')$ decrease to zero for $x \to \infty$, so that the steady density and mean velocity are recovered. The corrections $(\phi',\ u'_x,\ u'_y,\ h')$ are calculated in the present subsection by solving (3.22). The corrections due to incompressibility for the velocity fields $u''_x,\ u''_y$ are calculated in the next subsection using (3.24).

For the steady flow, the boundary condition at the top surface is the zero shear stress condition,

$$\frac{\mathrm{d}\bar{u}_x}{\mathrm{d}y} = 0 \quad \text{at } y = \bar{h}. \tag{4.5}$$

At the bottom surface at $y = 0$, we use a simple slip length approximation for the boundary condition,

$$\bar{u}_x = \beta\bar{h}\frac{\partial\bar{u}_x}{\partial y}, \tag{4.6}$$

where $\bar{h}$ is the height of the steady and fully developed flow, and $\beta\bar{h}$ is the slip length (it is convenient to define β as a dimensionless constant for the following analysis). The no-slip condition is recovered for $\beta = 0$, while the limit $\beta \to \infty$ corresponds to the zero shear stress condition.

For a steady, fully developed and incompressible flow, the governing equations (3.14) and (3.15) and boundary conditions (4.5) and (4.6) can be solved to obtain the Bagnold profile,

$$\bar{u}_x^B = \frac{5\bar{u}}{3}(1 - (1 - (y/\bar{h}))^{3/2}) + \bar{u}_s, \tag{4.7}$$

where $\bar{u}_s$ is the slip velocity at the bottom, $\bar{u} + \bar{u}_s$ is the height-averaged velocity, $\bar{u}$ can be calculated in terms of the gravitational acceleration and the Bagnold coefficients from (3.14),

$$\bar{u} = \frac{2}{5}\sqrt{\frac{\bar{\rho}g_x\bar{h}^3}{\bar{B}_{xy}}}, \tag{4.8}$$

where $\bar{\rho}$ is the constant density, and the slip velocity is related to the velocity gradient at the bottom through the boundary condition (4.6),

$$\bar{u}_s = \frac{5\beta\bar{u}}{2}. \tag{4.9}$$

The constant mean volume fraction $\bar{\phi}$ is defined by the relation,

$$\frac{\bar{B}_{xy}}{\bar{B}_{yy}} = \frac{B_{xy}(\bar{\phi})}{B_{yy}(\bar{\phi})} = \tan(\theta), \tag{4.10}$$

where θ is the angle of inclination.

https://doi.org/10.1017/jfm.2014.412 Published online by Cambridge University Press

In the linear approximation, the equations for u_x' and u_y' are

$$\bar{\rho}\left(\bar{u}_x\frac{\partial u_x'}{\partial x}+u_y'\frac{\mathrm{d}\bar{u}_x}{\mathrm{d}y}\right)=\frac{\partial}{\partial y}\left(B_{\phi xy}\phi'\left(\frac{\partial \bar{u}_x}{\partial y}\right)^2+2\bar{B}_{xy}\frac{\mathrm{d}\bar{u}_x}{\mathrm{d}y}\frac{\partial u_x'}{\partial y}\right), \tag{4.11}$$

$$0=\frac{\partial}{\partial y}\left(B_{\phi yy}\phi'\left(\frac{\partial \bar{u}_x}{\partial y}\right)^2+2\bar{B}_{yy}\frac{\mathrm{d}\bar{u}_x}{\mathrm{d}y}\frac{\partial u_x'}{\partial y}\right), \tag{4.12}$$

where we have used the expansion (3.19) for the Bagnold coefficients. The velocities u_x' and u_y' are expressed in terms on the stream function ψ' in a manner similar to (3.18),

$$u_x' = \frac{\partial \psi'}{\partial y}, \tag{4.13}$$

$$u_y' = -\frac{\partial \psi'}{\partial x}. \tag{4.14}$$

The slip condition (4.6) at the base $y=0$ can be expressed in terms of the stream function as

$$\frac{\partial \psi'}{\partial y}=\beta\bar{h}\frac{\partial^2\psi'}{\partial y^2}. \tag{4.15}$$

The zero normal velocity condition $u_y'=0$ at the base $y=0$ is

$$\frac{\partial \psi'}{\partial x}=0. \tag{4.16}$$

Without loss of generality, ψ' can be set equal to zero at the bottom surface, since it is defined only to within an additive constant. The linearised kinematic condition (3.25) is

$$\bar{u}_x|_{y=\bar{h}}\frac{\mathrm{d}h'}{\mathrm{d}x}=u_y'|_{y=\bar{h}} \tag{4.17}$$

where the expansion $h=\bar{h}+h'$ is used for the height, and $\bar{h}$ is the height of the fully developed flow. When the velocity u_y' is expressed in terms of the stream function, and integrated with respect to x, we obtain

$$h'=-\left.\frac{\psi'}{\bar{u}_x}\right|_{y=\bar{h}}. \tag{4.18}$$

Here, we have used the condition that both h' and ψ' are equal to zero in a fully developed flow in the limit $x\to\infty$. The zero strain rate condition (4.5) at $y=h$, linearised about $y=\bar{h}$, is

$$\frac{\partial^2\psi'}{\partial y^2}=0. \tag{4.19}$$

Equation (4.12) can be solved, subject to the boundary condition that the normal stress is zero at the free surface, to obtain an expression for ϕ' in terms of the strain rate,

$$\phi'=-\frac{2\bar{B}_{yy}}{B_{\phi yy}}\left(\frac{\mathrm{d}\bar{u}_x}{\mathrm{d}y}\right)^{-1}\frac{\partial u_x'}{\partial y}. \tag{4.20}$$

https://doi.org/10.1017/jfm.2014.412 Published online by Cambridge University Press

The above substitution for ϕ' is inserted into (4.11) to provide

$$\bar{\rho}\left(\bar{u}_x\frac{\partial u_x'}{\partial x}+u_y'\frac{\mathrm{d}\bar{u}_x}{\mathrm{d}y}\right)=2\mathscr{B}\frac{\partial}{\partial y}\left(\frac{\mathrm{d}\bar{u}_x}{\mathrm{d}y}\frac{\partial u_x'}{\partial y}\right). \tag{4.21}$$

Equation (4.14) is substituted into (3.21), and linearised in ψ', to obtain

$$\bar{\rho}\left(\bar{u}_x\frac{\partial^2\psi'}{\partial x\partial y}-\frac{\partial\psi'}{\partial x}\frac{\mathrm{d}\bar{u}_x}{\mathrm{d}y}\right)=2\mathscr{B}\frac{\partial}{\partial y}\left(\frac{\mathrm{d}\bar{u}_x}{\mathrm{d}y}\frac{\partial^2\psi'}{\partial y^2}\right). \tag{4.22}$$

Equation (4.22) has been simplified by noting that $(g_x+(g_y\bar{B}_{xy}/\bar{B}_{yy}))=0$ for the flow down an inclined plane. Using (4.7) for the mean velocity $\bar{u}_x$, and using the scaled y coordinate $y^\dagger=(y/\bar{h})$, (4.22) can be simplified to

$$\left(\bar{u}_x^*\frac{\partial^2\psi'}{\partial x\partial y^\dagger}-\frac{\partial\psi'}{\partial x}\frac{\mathrm{d}\bar{u}_x^*}{\mathrm{d}y^\dagger}\right)=\frac{2\mathscr{B}}{\bar{\rho}\bar{h}^3}\frac{\partial}{\partial y^\dagger}\left(\frac{\mathrm{d}\bar{u}_x^*}{\mathrm{d}y^\dagger}\frac{\partial^2\psi'}{\partial y^{\dagger 2}}\right), \tag{4.23}$$

where

$$\bar{u}_x^*=\frac{1-(1-y^\dagger)^{3/2}}{3}+\frac{\beta}{2}, \tag{4.24}$$

for the Bagnold profile, (4.7). If we define the scaled x coordinate as

$$x^\dagger=\frac{x\mathscr{B}}{\bar{\rho}\bar{h}^3}, \tag{4.25}$$

then the equation for the stream function becomes

$$\left(\bar{u}_x^*\frac{\partial^2\psi'}{\partial x^\dagger\partial y^\dagger}-\frac{\mathrm{d}\bar{u}_x^*}{\mathrm{d}y^\dagger}\frac{\partial\psi'}{\partial x^\dagger}\right)=2\frac{\partial}{\partial y^\dagger}\left(\frac{\mathrm{d}\bar{u}_x^*}{\mathrm{d}y^\dagger}\frac{\partial^2\psi'}{\partial y^{\dagger 2}}\right). \tag{4.26}$$

Equation (4.25) indicates that the length scale for the flow development in the x direction is

$$L=\frac{\bar{\rho}\bar{h}^3}{\mathscr{B}}. \tag{4.27}$$

It is useful to reiterate that the particle mass is assumed to be equal to 1 in all of the calculations, and therefore the Bagnold coefficients have dimensions of inverse length. The ratio of the length for flow development and the layer height is

$$\frac{L}{\bar{h}}=\frac{\bar{\rho}d^3}{d\mathscr{B}}\frac{\bar{h}^2}{d^2}, \tag{4.28}$$

where d is the particle diameter. In the above equation ρd^3 is $O(1)$ for dense granular flows. If we assume that $\bar{B}_{\phi xy}$ and $\bar{B}_{\phi yy}$ are comparable in magnitude, and $\tan(\theta)$ is $O(1)$, the development length is large compared with the layer height h for

$$\frac{\bar{h}}{d}\gg(d\bar{B}_{xy})^{1/2}. \tag{4.29}$$

An extended discussion and numerical evaluation of the development length is provided in § 7.

https://doi.org/10.1017/jfm.2014.412 Published online by Cambridge University Press

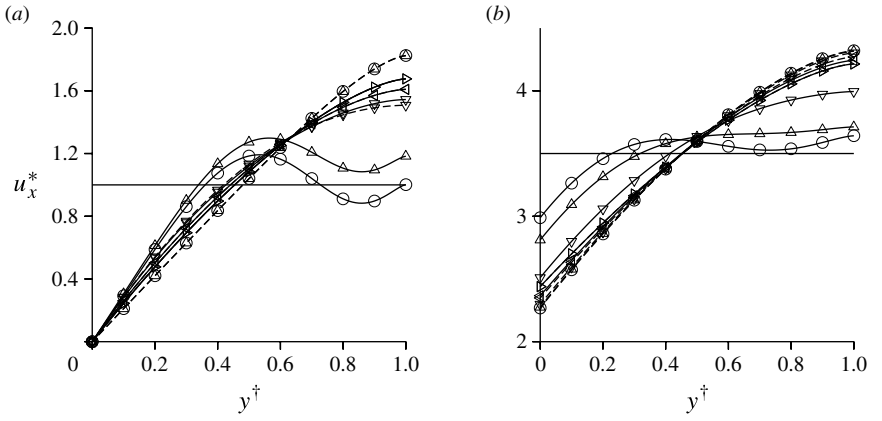


FIGURE 2. The developing velocity profiles $u_x^* = (u_x/\bar{u})$ as a function of $(y/\bar{h})$ at $x^\dagger = 0.01$ (○), $x^\dagger = 0.03$ (△), $x^\dagger = 0.1$ (▽), $x^\dagger = 0.3$ (◁), $x^\dagger = 1.0$ (▷) for $\beta = 0$ (*a*) and $\beta = 1.0$ (*b*). Here, $\bar{u}$ is the difference between the height averaged velocity and the slip velocity, the dashed lines show the solutions including one eigenfunction in the expansion, and the solid lines show the solutions including three eigenfunctions in the expansion in (B 20). The horizontal solid lines show the initial velocity profiles.

The detailed procedure for solving the (4.26) is provided in appendix B. A separation-of-variables procedure is used, where the solution for the transient part of the stream function is the product of a coefficient A_i, an exponentially decreasing function in the x direction, $\exp(-\alpha_i x^\dagger)$, and a function in the y direction, $Y_i(y^\dagger)$, that satisfies the boundary conditions. The boundary conditions are satisfied only for discrete eigenvalues α_i, all of which are negative and are increasing in magnitude as i increases. When ordered according to increasing magnitude, the first eigenvalue α_1 has a magnitude approximately 10 times less than the next highest eigenvalue. Therefore, at late times, it is possible to truncate the series at just the first term in the expansion. The eigenvalues asymptote to a constant value for $\beta \to 0$. For large β, the magnitude of α_1 decreases as β^2, while the magnitudes of all other eigenvalues decrease as β. The coefficients A_i can be determined from the initial plug velocity profile at $x^\dagger = 0$ using orthogonality relations.

The developing velocity profiles are shown at different stream-wise locations in figures 2 and 3. A salient feature of the developing profile is the convergence of the series expansion in (B 20), where the solution including three terms in the series is compared with that including just one term. Convergence is poor at upstream locations $x^\dagger = 0.01$ and $x^\dagger = 0.03$ for $\beta = 0.0$ and 1.0 and at $x^\dagger = 0.1$ and 0.3 at $\beta = 10.0$, where there is a significant difference due to the second and third terms in the series. For $\beta = 0$ and 1.0 and for $x^\dagger = 0.1$ and greater, the inclusion of just the first term provides a good approximation of the solution, and the contribution of the second and third terms is numerically small, indicating that the series has converged. This is due to the rather large numerical value of the first eigenvalue and the large difference between the first and second eigenvalues shown in figure 13. For $\beta = 10$, the first term in the series provides a good approximation for $x^\dagger = 1.0$ or larger, due to the smaller numerical value of the eigenvalue as shown in figure 13.

The spatial rate of relaxation of the velocity profile to the fully developed profile is proportional to the smallest eigenvalue α_1 for large $x^\dagger$, which decreases as the slip parameter β increases. This suggests that the relaxation to the final steady flow should

https://doi.org/10.1017/jfm.2014.412 Published online by Cambridge University Press

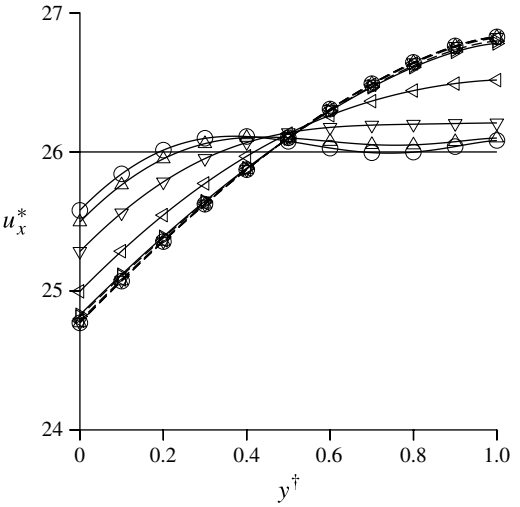


FIGURE 3. The developing velocity profiles $u_x^* = (u_x/\bar{u})$ as a function of $(y/\bar{h})$ at $x^\dagger = 0.1$ (○), $x^\dagger = 0.3$ (△), $x^\dagger = 1.0$ (▽), $x^\dagger = 3.0$ (◁), $x^\dagger = 10.0$ (▷) for $\beta = 10.0$. Here, $\bar{u}$ is the difference between the height averaged velocity and the slip velocity, the dashed lines show the solutions including one eigenfunction in the expansion, and the solid lines show the solutions including three eigenfunctions in the expansion in (B 20). The horizontal solid line shows the initial velocity profile.

be slower for higher values of β. This can be quantified by defining a development length $L^*_{0.99}$, which is the downstream distance at which the depth-averaged mean square difference between the velocity profile and the Bagnold profile is 1 % of the mean velocity,

$$\int_0^1 \mathrm{d}y^\dagger \, \frac{(u_x(x^\dagger = L^*_{0.99}, y^\dagger) - \bar{u}_x^B(y^\dagger))^2}{\bar{u}^2} = 0.01, \tag{4.30}$$

where $\bar{u}_x^B$ is the Bagnold profile (4.7). This length is shown as a function of the slip parameter β in figure 4. The scaled developing length is numerically small (approximately 0.1) for a rough base with a no-slip condition at the base, but it increases rapidly as the slip parameter β increases, primarily due to the sharp decrease in the lowest eigenvalue α_1 in figure 13. However, the relative difference between the developing and fully developed profiles also decreases as β increases, due to the increase in the ratio of the slip velocity and the mean velocity.

The scaled variation in height, $(h'/\bar{h})$, can be calculated from equation (B 2). This height variation is shown as a function of the scaled stream-wise distance $x^\dagger$ in figure 5. The initial condition is a plug flow with the same average velocity as the steady state flow, so h' is equal to zero at $x^* = 0$ by construction. Due to the deceleration at the base, the average velocity first decreases with increasing $x^\dagger$, resulting in an increase in height, followed by a further decrease as the final steady-state Bagnold profile is attained. The maximum value of $(h'/\bar{h})$ decreases as the slip parameter β increases, but the maximum occurs at a higher value of $x^\dagger$ as β increases. This is because the largest eigenvalue α_1 in the expansion decreases as β increases as shown in figure 13 in appendix B, and so the spatial rate of decay of the height variation decreases as β increases. The height variation is also numerically small, and $(h'/\bar{h})$ has a maximum value of approximately 0.2 for $\beta = 0$. Although

https://doi.org/10.1017/jfm.2014.412 Published online by Cambridge University Press

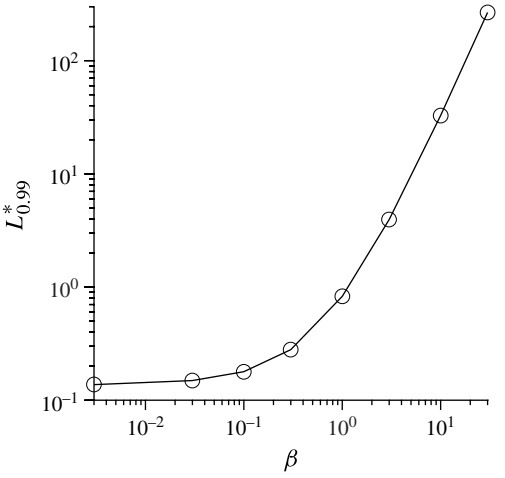


FIGURE 4. The developing length $L^*_{0.99}$ as a function of the slip parameter β.

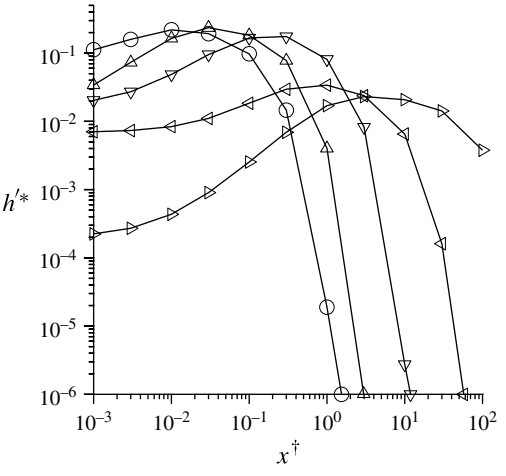


FIGURE 5. The variation of the scaled height modification $h'^* = (h'/\bar{h})$ as a function of the downstream distance $x^\dagger$ for $\beta = 0$ (○), 0.3 (△), 1.0 (▽), 3.0 (◁) and 10.0 (▷).

the initial condition (B 22) is a plug flow with the same average velocity as the final steady state, the numerical solution does not decrease to zero at small $x^\dagger$ because we have used only the first three eigenfunctions in the expansion (B 2). Due to the truncation of the series, the results for h' are not accurate for very small values of $x^\dagger$, but are accurate for $x^\dagger > \alpha_3^{-1}$, where α_3 is the eigenvalue with the third lowest magnitude in figure 13.

The correction to the volume fraction due to the flow can now be calculated using (4.20). The correction to the volume fraction can be expressed as

$$\phi' = \frac{B_{yy}}{B_{\phi yy}} \sum_i \phi_i^{*'}(y^\dagger) \exp(-\alpha_i x^\dagger), \tag{4.31}$$

where

$$\phi_i^{*'}(y^\dagger) = -\frac{4A_i}{5\sqrt{1-y^\dagger}} \frac{\mathrm{d}^2 Y_i}{\mathrm{d}y^{\dagger 2}}. \tag{4.32}$$

https://doi.org/10.1017/jfm.2014.412 Published online by Cambridge University Press

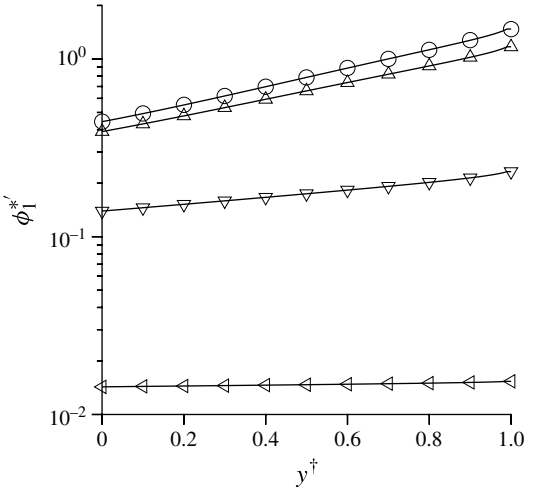


FIGURE 6. The correction to the volume fraction, $\phi_1^{*'}$ (4.32) as a function of $y^\dagger$ for $\beta = 0$ (○), $\beta = 0.1$ (△), $\beta = 1.0$ (▽), $\beta = 10.0$ (◁).

The function $\phi_1^{*'}(y^\dagger)$ is shown as a function of $y^\dagger$ in figure 6. The solutions for $i = 2, 3$, which are not shown for conciseness, follow similar trends. It is observed that the correction to the volume fraction decreases by two orders of magnitude as β increases from 0 to 10, indicating that volume fraction variations are significant for rough bases but may not be as significant for smooth bases. The volume fraction variation is smooth throughout the domain, and there is no divergence either at the base or at the free surface. The volume fraction increases with height, as intuitively expected, due to the decrease of the granular temperature with height. It should be noted that we have not incorporated the boundary layer at the top free surface, where the temperature equation has to be solved. Due to this, the present calculation does not recover the sharp drop in the volume fraction at the free surface. Finally, it is important to note that the scaled volume fraction in figure 6 has to be multiplied by $(\bar{B}_{yy}/\bar{B}_{\phi yy})$, in order to obtain the actual variation in the volume fraction. This factor, called the Compressibility number, is typically small for dense granular flows, as discussed in § 7.

4.2. *Effect of compressibility*

The correction to the velocity field due to compressibility is calculated using the mass conservation (3.16), which is more conveniently expressed in terms of the volume fraction ϕ (which differs from the density by a constant factor of $(\pi d^3/6)$, where d is the particle diameter). In the linear approximation, the mass conservation equation (3.16) is

$$\bar{\phi}\left(\frac{\partial u_x''}{\partial x} + \frac{\partial u_y''}{\partial y}\right) + \bar{u}_x \frac{\partial(\phi' + \phi'')}{\partial x} = 0. \tag{4.33}$$

Here, the (3.16) is simplified because the only non-zero component of the velocity $\bar{u}_x$ is a function of y, and $\bar{\phi}$ is a constant. When we neglect ϕ'' in comparison with ϕ' in the second term on the left-hand side of (4.33), the equation for u_x'' and u_y'' is

$$\frac{\partial u_x''}{\partial x} + \frac{\partial u_y''}{\partial y} = -\frac{\bar{u}_x}{\bar{\phi}} \frac{\partial \phi'}{\partial x}. \tag{4.34}$$

https://doi.org/10.1017/jfm.2014.412 Published online by Cambridge University Press

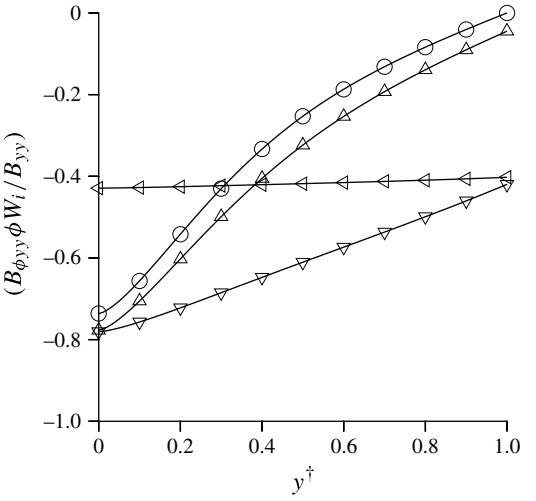


FIGURE 7. The solutions $(\bar{B}_{\phi yy}\bar{\phi}W_i(y^\dagger)/\bar{B}_{yy})$ of (B 29) with boundary conditions (B 31)–(B 33) for $\beta = 0$ (○), $\beta = 0.1$ (△), $\beta = 1.0$ (▽), $\beta = 10.0$ (◁).

The combined momentum balance equation for u_x'' and u_y'', similar to (4.21) but with (u_x'', u_y'') replacing (u_x', u_y'),

$$\bar{\rho}\left(\bar{u}_x\frac{\partial u_x''}{\partial x} + u_y''\frac{\mathrm{d}\bar{u}_x}{\mathrm{d}y}\right) = 2\mathscr{B}\frac{\partial}{\partial y}\left(\frac{\mathrm{d}\bar{u}_x}{\mathrm{d}y}\frac{\partial u_x''}{\partial y}\right). \tag{4.35}$$

In simplifying the above equation, we have not included the variations in the volume fraction on the left-hand side, and thereby neglected terms of $O(\phi' u_x')$ and $O(\phi' u_y')$. These are neglected in comparison with the correction to the mass conservation equation (4.34), which is $O(\bar{u}_x\phi')$.

Equation (4.35) is solved for the velocity profiles as shown in appendix B. The solution is of the form

$$u_x'' = \sum_i \exp(-\alpha_i x^\dagger) W_i(y^\dagger) \tag{4.36}$$

where α_i are the eigenvalues for the incompressible flow equations discussed in the previous subsection, and the functions $W_i(y^\dagger)$ are obtained by solving (B 29) in appendix B. Since the inhomogeneous term in (B 29) is proportional to $(\bar{B}_{yy}/\bar{\phi}\bar{B}_{\phi yy})$, the solution can be conveniently expressed as $(\bar{B}_{\phi yy}\bar{\phi}W_i/\bar{B}_{yy})$. These solutions are shown, for the lowest eigenvalue α_1 and for different values of the slip parameter β in figure 7. The corrections to the velocity u_x are negative, indicating that the flow is retarded when the effect of compressibility is included. The solutions are also all bounded, and show less variation as β is increased, indicating that compressibility effects do not qualitatively alter the nature of the velocity profiles. The numerical value of the ratio $(\bar{B}_{yy}/\bar{\phi}\bar{B}_{\phi yy})$, referred to as the compressibility number, is discussed in § 7.

5. Momentum boundary layer

The configuration consists of a granular flow of height h on a smooth base for $x < 0$, where there is slip at the base and the flow in the bulk is a slowly evolving

https://doi.org/10.1017/jfm.2014.412 Published online by Cambridge University Press

plug flow $u_x = U(x)$. There is a rough base with zero velocity boundary condition for $x > 0$, and we examine the development of the boundary layer for $x > 0$. The boundary layer equations for the granular flow are (3.23) and (3.24) where the volume fraction perturbation (3.20) is approximated as

$$\phi' = -\frac{\bar{\rho} g_y h}{\bar{B}_{\phi yy}(\partial u_x/\partial y)^2} - \frac{\bar{B}_{yy}}{\bar{B}_{\phi yy}} = \phi^\dagger - \frac{\bar{B}_{yy}}{\bar{B}_{\phi yy}}, \tag{5.1}$$

where $\phi^\dagger$ is the part of the correction to the volume fraction, ϕ', which depends on the strain rate. In (5.1), it is assumed that the flow height h is large compared with the boundary layer thickness, and the perturbation to the mass density within the boundary layer is neglected in comparison to the mean density $\bar{\rho}$. Equation (5.1) is inserted into the x momentum equation (3.24) to obtain

$$\rho\left(u_x\frac{\partial u_x}{\partial x} + u_y\frac{\partial u_x}{\partial y}\right) = \frac{\mathscr{B}}{\rho}\frac{\partial}{\partial y}\left(\left(\frac{\partial u_x}{\partial y}\right)^2\right) + g_x + \frac{g_y\bar{B}_{\phi xy}}{\bar{B}_{\phi yy}}, \tag{5.2}$$

where $\mathscr{B} = (\bar{B}_{xy} - \bar{B}_{yy}\bar{B}_{\phi xy}/\bar{B}_{\phi yy})$. For consistency with the outer flow solutions, we require that $g_x + (g_y\bar{B}_{\phi xy}/\bar{B}_{\phi yy}) = U(\mathrm{d}U/\mathrm{d}x)$. With this substitution, the equation for the velocity u_y is

$$u_y = \left(\frac{\partial u_x}{\partial y}\right)^{-1}\left[U\frac{\mathrm{d}U}{\mathrm{d}x} - u_x\frac{\partial u_x}{\partial x} + \frac{\mathscr{B}}{\rho}\frac{\partial}{\partial y}\left(\left(\frac{\partial u_x}{\partial y}\right)^2\right)\right]. \tag{5.3}$$

The last term on the right-hand side of the above equation contains inverse of the density ρ, which can be written in the linearisation approximation as $\rho^{-1} = \bar{\rho}^{-1}(1 + \phi'/\bar{\phi})^{-1}$. Using this approximation, the expression for the velocity is

$$u_y = \left(\frac{\partial u_x}{\partial y}\right)^{-1}\left(U\frac{\mathrm{d}U}{\mathrm{d}x} - u_x\frac{\partial u_x}{\partial x}\right) + \frac{2\mathscr{B}}{\bar{\rho}}\left(1 + \frac{\phi'}{\bar{\phi}}\right)^{-1}\frac{\partial^2 u_x}{\partial y^2}. \tag{5.4}$$

This is substituted into the mass conservation equation, (3.24). Dividing throughout by $-(1 + \phi'/\bar{\phi} + 2\phi^\dagger/\bar{\phi})$, and after some simplification, we obtain

$$\begin{aligned}&\left(u_x\left(\frac{\partial u_x}{\partial y}\right)^{-1}\frac{\partial^2 u_x}{\partial x\partial y} + \left(\frac{\partial u_x}{\partial y}\right)^{-2}\left(\frac{\partial^2 u_x}{\partial y^2}\right)\left(U\frac{\mathrm{d}U}{\mathrm{d}x} - u_x\frac{\partial u_x}{\partial x}\right) + l^2\frac{\partial^3 u_x}{\partial y^3}\right)\\ &+ l^2\left(1 + \frac{\phi'}{\bar{\phi}} + \frac{2\phi^\dagger}{\bar{\phi}}\right)^{-1}\left[-\left(\frac{\phi'}{\bar{\phi}} + \frac{2\phi^\dagger}{\bar{\phi}}\right)\frac{\partial^3 u_x}{\partial y^3}\right.\\ &\left.+ \frac{4\phi^\dagger}{\bar{\phi}}\left(1 + \frac{\phi'}{\bar{\phi}}\right)^{-1}\left(\frac{\partial u_x}{\partial y}\right)^{-1}\left(\frac{\partial^2 u_x}{\partial y^2}\right)^2\right] = 0,\end{aligned} \tag{5.5}$$

where the length scale l is

$$l = \sqrt{\frac{2\mathscr{B}}{\bar{\rho}}}. \tag{5.6}$$

The first term on the left-hand side of (5.5) is the leading-order equation in the incompressible limit, while the second term is the correction due to the compressibility

https://doi.org/10.1017/jfm.2014.412 Published online by Cambridge University Press

of the flowing material. The leading-order equation is first solved using a similarity solution procedure.

In order to obtain a similarity solution, the similarity variable η is defined as

$$\eta = y/\delta(x), \tag{5.7}$$

where $\delta(x)$ is the boundary layer thickness. The x velocity is defined in terms of the similarity variable as

$$u_x(x, y) = U(x)s(\eta). \tag{5.8}$$

Using this substitution, the leading-order contribution to the conservation equation (the first term on the left-hand side of (5.5)) becomes

$$\frac{\mathrm{d}U}{\mathrm{d}x}\left(\frac{s''(s^2-1)}{s'^2} - s\right) + \frac{U}{\delta}\frac{\mathrm{d}\delta}{\mathrm{d}x}s + \frac{l^2U}{\delta^3}s''' = 0, \tag{5.9}$$

where the primes denote derivatives with respect to η. The above equation can be multiplied by (δ^3/Ul^2) to obtain

$$F(x)\left(\frac{s''(s^2-1)}{s'^2} - s\right) + G(x)s + s''' = 0, \tag{5.10}$$

$$F(x) = \frac{\delta^3}{l^2U}\frac{\mathrm{d}U}{\mathrm{d}x}, \tag{5.11}$$

$$G(x) = \frac{\delta^2}{l^2}\frac{\mathrm{d}\delta}{\mathrm{d}x}. \tag{5.12}$$

It can easily be verified that the (5.10) is consistent with the Falkner–Skan equation for the scaled stream function, $f = (\psi/U\delta)$, obtained from the momentum conservation equation (3.22) and the consistency condition $U(\mathrm{d}U/\mathrm{d}x) = g_x + (g_y\bar{B}_{xy}/\bar{B}_{yy})$. The resulting equation for the scaled stream function is

$$f'''f'' + F(x)(1 - f'^2 + ff'') + G(x)ff'' = 0. \tag{5.13}$$

To verify the equivalence of (5.10) and (5.13), divide (5.13) by f'' and take the derivative with respect to η; the resulting equation is identical to (5.10) with $s = f'$.

A similarity solution exists for (5.10) only if F and G are independent of x. The boundary layer thickness is determined by considering

$$\frac{1}{l^2}\frac{\mathrm{d}\delta^3}{\mathrm{d}x} = 3G. \tag{5.14}$$

As in standard boundary layer theories, the term on the right-hand side of (5.14) can be set equal to 1 without loss of generality, and the boundary layer thickness becomes

$$\delta = (l^2x)^{1/3}. \tag{5.15}$$

The second condition on the mean velocity (5.12) reduces to

$$\frac{x}{U}\frac{\mathrm{d}U}{\mathrm{d}x} = F. \tag{5.16}$$

https://doi.org/10.1017/jfm.2014.412 Published online by Cambridge University Press

This requires that the mean velocity has to have a power law dependence on the stream-wise coordinate x, in order to admit boundary layer solutions,

$$U = U_0 x^F. \tag{5.17}$$

The differential equation for the scaled stream function then reduces to

$$F\left(\frac{s''(s^2-1)}{s'^2} - s\right) + (1/3)s + s''' = 0. \tag{5.18}$$

The velocity profiles which satisfy (5.17) are the same as the corner flows that provide self-similar solutions to the Falkner–Skan boundary layer equations for Newtonian fluids. The case $F = 0$ is the flow over a flat plate where the velocity is a constant far from the surface, $F = 1$ corresponds to a stagnation point flow. The case $F > 1$ corresponds to the accelerating flow in a corner with angle less than $(\pi/2)$, while $0 < F < 1$ corresponds to the accelerating flow in a corner with angle between $(\pi/2)$ and π. For $F < 0$, the corner has angle greater than π and the flow decelerates (velocity decreases with stream-wise distance), and $F = -1/2$ for the maximum possible corner angle 2π (flow around the edge of a flat plate). In contrast to the boundary layer equations for Newtonian fluids, the granular dynamics equations predict that the boundary layer thickness increases as $x^{1/3}$ for all velocity profiles.

Numerical solutions for (5.18) are more easily obtained starting from (5.13) instead. These are solved in the domain $0 \leqslant \eta \leqslant 10$, using the no-slip conditions $u_x = u_y = 0$ at $\eta = 0$, which reduce to $f(\eta) = f'(\eta) = 0$, and the zero stress condition $f''(\eta) = 0$ at $\eta = 10$. A fourth-order Runge–Kutta method is used for numerical integration with 10^4 intervals in the domain $0 \leqslant \eta \leqslant 10$, and a shooting technique is used to enforce the boundary condition at $\eta = 10$. The case $F = 0$ (with a constant outer flow velocity) is a special case, where the (5.18) reduces to a linear equation which does not have analytical solutions satisfying all boundary conditions. For all non-zero values of F, (5.18) is a nonlinear equation which has to be solved numerically. The numerical solutions for the nonlinear equation are shown in figure 8, along with the numerical solution obtained for $F = 0$ by interpolating the solutions for $F = 0.01$ and $F = -0.01$. The function $s'(\eta)$ at $\eta = 0$, which is proportional to the velocity gradient at the base, is shown as a function of F in figure 9. As in the case of momentum boundary layers in Newtonian fluids, we find that the slope of the velocity profile decreases and the velocity gradient at the base decreases as F decreases, from a maximum of approximately 2.26 at $F = 5.0$, to approximately 0.5 at $F = 0.0$. As F is further decreased, it is observed that $s'(\eta)$ (and therefore the shear stress at the surface) decreases to 0 at approximately $F = -0.0593$. In the case of a boundary layer flow of a Newtonian fluid, a further decrease in F should result in a negative velocity close to the surface, and a zone of recirculation close to the surface. That regime is not directly accessible in the present analysis, since the strain rate was assumed positive while simplifying the equations. However, in the following analysis, there is a hint that the flow separation phenomenon may be qualitatively different in a granular flow in comparison with the flow of a Newtonian fluid. The following calculations show that the boundary layer thickness appears to diverge for a decelerating flow with $F = -0.0593$, indicating that the boundary layer approximation may not be valid.

Quantitative measures of the boundary layer thickness can be defined in a manner similar to those for the Falkner–Skan solutions. The boundary layer thickness $\delta_{0.99}$ is defined as the height at which the stream-wise velocity is 0.99 times the free stream

https://doi.org/10.1017/jfm.2014.412 Published online by Cambridge University Press

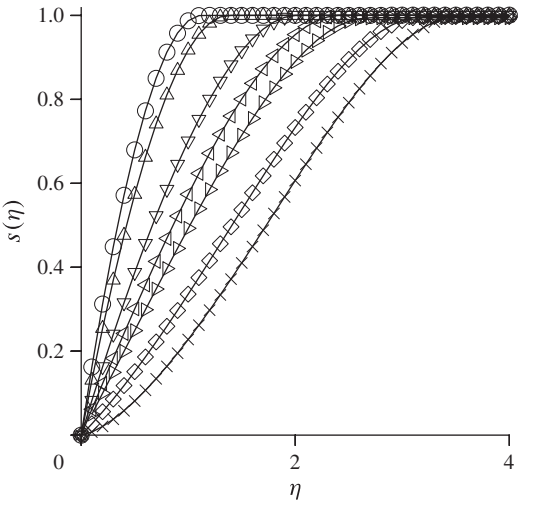


FIGURE 8. The solutions for $(u(x, y)/U(x)) = s(\eta)$ as a function of η for $F = 2.0$ ($\bigcirc$), $F = 1.0$ ($\triangle$), $F = 0.2$ (∇), $F = 0.05$ ($\triangleleft$), $F = 0.0$ ($\triangleright$, obtained by interpolation of the solutions for $F = -0.01$ and $F = 0.01$), $F = -0.05$ ($\diamond$), $F = -0.0592$ ($\times$).

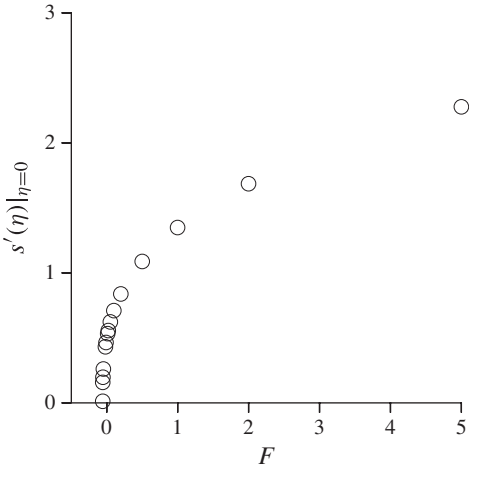


FIGURE 9. The scaled strain rate $s'(\eta)$ at $\eta = 0$ as a function of F.

value. The displacement and the momentum thickness for the boundary layer flow are defined as

$$\delta_1 = \int_0^\infty \mathrm{d}\eta \left(1 - \frac{u_x}{U}\right) = \int_0^\infty \mathrm{d}\eta (1 - s(\eta)), \tag{5.19}$$

$$\delta_2 = \int_0^\infty \mathrm{d}\eta \frac{u_x}{U} \left(1 - \frac{u_x}{U}\right) = \int_0^\infty \mathrm{d}\eta\, s(\eta)(1 - s(\eta)). \tag{5.20}$$

The scaled boundary layer thickness $\delta^*_{0.99} = (\delta_{0.99}/(l^2 x)^{1/3})$, and the displacement and momentum thickness, are shown as a function of F in figure 10. All of these boundary layer thicknesses tend to a finite limit for large F, but appear to diverge in

https://doi.org/10.1017/jfm.2014.412 Published online by Cambridge University Press

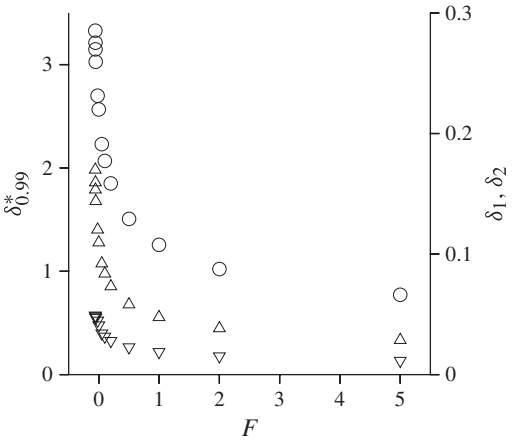


FIGURE 10. The scaled boundary layer thickness $\delta^*_{0.99} = (\delta_{0.99}/(l^2x)^{1/3})$ ○, the displacement thickness δ_1 △ and the momentum thickness δ_2 ▽ (5.20) as a function of the exponent F.

as F approaches -0.0593 where the shear stress decreases to zero. From the data in figure 10, it is not clear whether there is a divergence in the boundary layer thickness, and more study is required to resolve this issue. However, if there is a divergence, it indicates a breakdown of the assumption that the boundary layer thickness is much smaller than the flow height; this is in contrast to the boundary layer flow of a Newtonian fluid, where there is no divergence in the boundary layer thickness.

5.1. *Effect of compressibility*

There are two important compressibility effects that restrict the validity of the boundary layer theory in the previous subsection, which are the assumption of small ϕ' and the stream-wise growth of the first correction to the boundary layer equations. First, we return to the expression (5.1) for ϕ', which can be written in terms of $s(\eta)$ as

$$\phi' = -\frac{\bar{\rho} g_y h \delta^2}{\bar{B}_{\phi yy} U^2 (s')^2} - \frac{\bar{B}_{yy}}{\bar{B}_{\phi yy}}. \tag{5.21}$$

In the analysis, we had assumed $(\phi'/\bar{\phi}) \ll 1$; this assumption requires that $(\bar{\rho}|g_y|h\delta^2/\bar{\phi}\,\bar{B}_{\phi yy}\,U^2(s')^2) \ll 1$. However, the solution of the boundary layer equations satisfies $s'(\eta) \to 0$ as $\eta \to \infty$. For the boundary layer solution to be a good approximation, it is necessary to satisfy two conditions, $s' \ll 1$ and $s' \gg (\bar{\rho}|g_y|h\delta^2/\bar{\phi}\bar{B}_{\phi yy}U^2)^{1/2}$. For both limits $s' \ll 1$ and $(\phi'/\bar{\phi}) \ll 1$ to be simultaneously valid, a necessary condition is that $h \ll h_0$, where the length scale h_0 is

$$h_0 = \frac{\bar{B}_{\phi yy} U_0^2}{\bar{\rho}|g_y| l^{4/3}} x^{2F-2/3}. \tag{5.22}$$

Thus, there is an upper bound on the height h for the validity of the boundary layer solutions in the previous section.

The correction to the volume fraction ϕ' also diverges for the case where the shear stress at the surfaces decreases to zero at $F = -0.593$, as discussed in the previous section. However, this divergence has its origins in the neglect of the conduction term

https://doi.org/10.1017/jfm.2014.412 Published online by Cambridge University Press

in the energy balance equation. When the strain rate is zero, the energy conduction cannot be neglected in comparison to the source of energy, and the complete energy balance equation has to be solved near the bottom surface to determine the granular temperature. This solution can be used to cut-off the divergence in ϕ' at the bottom surface.

Next, we examine the correction to the velocity profile due to volume fraction variations. The effect of compressibility is included using the following expansion for the velocity,

$$u_x = U(x)s(\eta) + A(x)q(\eta). \tag{5.23}$$

The above velocity is substituted into the (5.5), and the leading-order approximation for the velocity is subtracted from this, to obtain

$$\begin{aligned}&\frac{Al^2q'''}{\delta^3} - \frac{Aq}{\delta}\frac{\mathrm{d}\delta}{\mathrm{d}x} + \frac{\mathrm{d}A}{\mathrm{d}x}\left(\frac{s(s'q' - s''q)}{s'^2}\right)\\ &+ \frac{A}{U}\frac{\mathrm{d}U}{\mathrm{d}x}\left(q\left(1 - \frac{ss''}{s'^2}\right) + q'\left(\frac{2s''(s^2-1)}{s'^3} - \frac{s}{s'}\right) + q''\left(\frac{1-s^2}{s'^2}\right)\right)\\ &- \frac{2\bar{\rho}g_y hl^2}{\bar{B}_{\phi yy}U\delta s'^2}\left[-3s''' + \frac{4s''^2}{s'}\right] + \frac{\bar{B}_{\phi yy}l^2Us'''}{\bar{B}_{yy}\delta^3} = 0.\end{aligned} \tag{5.24}$$

Here, we have neglected terms of $O(\phi'^2)$ and smaller in the second term on the right-hand side of (5.5) in the limit $\phi' \ll 1$.

The last two terms on the left-hand side of (5.24) are the inhomogeneous terms. The last term admits a similarity solution only if $A(x) \sim x^F$ has the same scaling as the mean velocity. Since this inhomogeneous solution is of the same form as the leading-order solution, this can be easily incorporated into the leading-order solution by just renormalising the value of the length l, and so we do not pursue this further. The correction due to the second last term on the right-hand side of (5.24) has, in general, a different stream-wise variation than the leading-order solution s. It can easily be verified that (5.24) admits a similarity solution only if

$$A(x) = -\frac{\bar{\rho}g_y hl^{4/3}}{B_{\phi yy}U_0}x^{2/3-F}. \tag{5.25}$$

Note that g_y is negative in the present configuration, and so A is positive. With this similarity form, the (5.24) (neglecting the last term on the left) becomes

$$\begin{aligned}&q''' - \frac{q}{3} + \left(\frac{2}{3} - F\right)\left(\frac{s(s'q' - s''q)}{s'^2}\right) + F\left(q\left(1 - \frac{ss''}{s'^2}\right)\right.\\ &\left.+ q'\left(\frac{2s''(s^2-1)}{s'^3} - \frac{s}{s'}\right) + q''\left(\frac{1-s^2}{s'^2}\right)\right) + 2\left[-3s''' + \frac{4s''^2}{s'}\right] = 0.\end{aligned} \tag{5.26}$$

The first correction to the velocity profile is smaller than the leading-order solution only if $A(x) \ll U(x)$ is satisfied. Using (5.25), the condition $A(x) \ll U(x)$ reduces to $h \ll h_0$, where h_0 is the length scale in (5.22). Thus, the condition for $A(x) \ll U(x)$ is identical to that required for $(\phi'/\bar{\phi}) \ll 1$. From (5.22), the length scale h_0 varies as $x^{2F-2/3}$. For $F > 1/3$, the length scale h_0 increases as x increases, and the boundary layer solution is valid only for a downstream locations $x \gg (\bar{\rho}|g_y|hl^{4/3}/\bar{B}_{\phi yy}U_0^2)^{(2F-2/3)^{-1}}$. In contrast, for $F < 1/3$, the length scale h_0 decreases as x increases, and the boundary

https://doi.org/10.1017/jfm.2014.412 Published online by Cambridge University Press

layer solution is valid only for upstream locations $x \ll (\bar{B}_{\phi yy} U_0^2/\bar{\rho}|g_y|hl^{4/3})^{(2/3-2F)^{-1}}$, while the approximation is not valid upstream. In either case, the assumption on $(\phi'/\bar{\phi}) \ll 1$ places a restriction on the validity of the solutions obtained in the previous subsection, even though the equations are well posed and the solutions do not contain any singularity in the domain. A more general framework, which does not assume $(\phi'/\bar{\phi}) \ll 1$, is required in order to obtain uniformly valid solutions throughout the domain.

6. Summary

A simplified set of mass and momentum conservation equations were derived for a shallow dense granular flow. The starting point were the kinetic-theory-based mass, momentum and energy equations, with a very general model for the stress tensor. The basic approximations are the 'shallow' approximation that the stream-wise length scale L is large compared with the cross-stream height h, and the 'dense' approximation that the volume fraction is close to the volume fraction for dynamical arrest. In the dense limit, the pair distribution function at contact in the Enskog theory is numerically large ($\chi \gg 1$), and the derivative of the pair distribution function is much larger than the pair distribution function, $(\mathrm{d}\chi/\mathrm{d}\phi) \gg (\chi/\phi)$. In addition, the pressure, viscosity, Burnett coefficient and thermal conductivity increase proportional to the pair distribution function χ. When the system size is large compared with the 'conduction length' (Kumaran 2008), the energy balance equation simplifies to an algebraic balance between the rate of energy production due to shear and energy dissipation due to inelastic collisions. In the shallow approximation with $h \ll L$, the largest contributions to the stress tensor reduce to the Bagnold form, $\sigma_{ij} = B_{ij}(\phi)(\partial u_x/\partial y)^2$, where x and y are the stream-wise and cross-stream directions, respectively, independent of the form of the constitutive relation used. Using a simple linear approximation for the Bagnold coefficients, $B_{ij}(\phi) = \bar{B}_{ij} + (\phi - \bar{\phi})\bar{B}_{\phi ij}$, the reduced set of (3.13) and (3.21) were obtained. Here, $\bar{\phi}$ is a reference volume fraction, $\bar{B}_{ij} = B_{ij}(\bar{\phi})$ and $\bar{B}_{\phi ij} = (\mathrm{d}B_{ij}/\mathrm{d}\phi)|_{\phi=\bar{\phi}}$. Equations (3.13) and (3.21) are similar to the boundary layer equations for the high-Reynolds-number flow of Newtonian fluids, but with the important difference that the stress is given by the Bagnold law $\sigma_{ij} = B_{ij}(\phi)(\partial u_x/\partial y)^2$. It should be noted that even in the incompressible limit, the equations do contain the effect of variations in the volume fraction on the Bagnold coefficients. The volume fraction variation is determined using the y momentum conservation equation (3.15), and this is inserted into the x momentum equation (3.14), so that the resulting set of 'shallow dense flow' (3.13) and (3.21) do not explicitly contain volume fraction. Apart from the density, there is only one parameter, $\mathscr{B}$, in (3.13) and (3.21), even though we started with a constitutive model which contained two Bagnold coefficients and their derivatives. Therefore, these equations provide an elegant and powerful framework for analysing shallow dense granular flows.

The important shortcoming of the present analysis is the ϕ expansion of the Bagnold coefficients in (3.19). Since the pair distribution function and the Bagnold coefficients exhibit a power law divergence near the volume fraction for arrested dynamics, a linear expansion is likely to be in error as the volume fraction for arrested dynamics is approached. A smooth spatial progression from a flowing layer to a static layer, as observed in many surface flows and rotating drum flows, cannot be modeled using a ϕ expansion of the Bagnold coefficients. Further work is required to extend the analysis to such types of flows.

We have also considered the corrections to these equations due to compressibility and non-parallel effects. The largest neglected term in the equations depends the

https://doi.org/10.1017/jfm.2014.412 Published online by Cambridge University Press

relative magnitudes of $(\chi/\phi(\mathrm{d}\chi/\mathrm{d}\phi))$ and (h/L). For $(\chi/\phi(\mathrm{d}\chi/\mathrm{d}\phi)) \gg (h/L)$ the largest correction to the dense shallow flow equations are due to compressibility effects in the mass conservation equation. The correction due to compressibility has been analysed in some detail for both the representative flows considered here. In the opposite limit, $(\chi/\phi(\mathrm{d}\chi/\mathrm{d}\phi)) \ll (h/L)$, the largest correction is due to non-parallel effects in an incompressible granular flow, which we have not analysed here.

The incompressible dense shallow flow equations were solved for the spatial development for the flow down an inclined plane from an initial plug flow to a fully developed Bagnold profile for a flowing layer with height h. A zero stress condition is applied at the free surface, and the slip at the base is given by a simple slip length model, where the slip length is assumed to be of the form βh, and β is a dimensionless parameter. An important simplification is the linearisation approximation where the Bagnold stress is linearised in the departure from the Bagnold profile. The linear equation was solved, subject to the boundary conditions, to obtain the eigenvalues for the spatial rate of development of the flow and the eigenfunctions for the departure from the steady-state Bagnold profiles. The lowest eigenvalue is about an order of magnitude smaller than the next higher eigenvalue, indicating that a single eigenfunction approximation is a good one in the late stages of flow. The lowest eigenvalue is finite when there is a no-slip condition at the base, but decreases as β^{-2} for $\beta \gg 1$.

The variations in volume fraction and the correction to the velocity profiles due to compressibility, were determined by incorporating the first correction to the mass and momentum equations. The corrections were found to be proportional to $(\bar{B}_{yy}/\bar{B}_{\phi yy})$. The volume fraction increases with height, consistent with the decrease of the granular temperature which is proportional to the square of the strain rate. Both the correction to the volume fraction and the correction to the velocity decrease by an order of magnitude when the scaled slip length increases from 0 to 10.

The second representative example considered here is the development of the momentum boundary layer at the base of the flow, when there is a discontinuous transition from a smooth base with a slip boundary condition to a rough base with a no-slip boundary condition. The prescribed 'free stream' velocity $U(x)$ far from the base is related the stream-wise and cross-stream acceleration due to gravity by the relation $g_x + (g_y\bar{B}_{xy}/\bar{B}_{yy}) = U(\mathrm{d}U/\mathrm{d}x)$. A similarity solution of the form $u_x = U(x)s(y/\delta(x))$ can be obtained only if the mean velocity is proportional to a power of the stream-wise distance, $U(x) = U_0x^F$, which are the potential flow solutions for the flow around a corner. The boundary layer thickness $\delta(x)$ increases proportional to $(l^2x)^{1/3}$, independent of the exponent F. Here, the material length scale $l = \sqrt{2\mathscr{B}/\bar{\rho}}$ depends only on the particle diameter and volume fraction through the Bagnold coefficients, and is independent of the flow velocity or the layer height. In contrast to the boundary layer solutions for Newtonian fluids, the boundary layer thickness does not depend on F, and it increases proportional to $x^{1/3}$ for all values of F. The boundary layer equations are slightly different from the Falkner–Skan equations for the boundary layer in a Newtonian fluid, due to the difference in the form of the stress tensor. However, the qualitative features of the solutions for $s(y/\delta)$ are similar to those in boundary layer theory for Newtonian fluids. As the exponent F decreases, the boundary layer thickness increases and the strain rate at the surface decreases. The strain rate decreases to zero for $F \approx -0.0593$, and the numerical results suggest that the boundary layer thickness diverges at this point, although further analysis is required to establish the divergence.

https://doi.org/10.1017/jfm.2014.412 Published online by Cambridge University Press

The effect of compressibility on the velocity profiles was also studied by calculating the first correction to the velocity profile due to volume fraction variations. It was found that the correction to the boundary layer equations due to volume fraction variations scales as $x^{2/3-2F}$ times the leading order solution. Due to this correction, there is a limit on the applicability of the leading order boundary layer equations. The boundary layer solutions are valid only for $h \ll h_0$, where the height h_0 (5.22) is proportional to $x^{2F-2/3}$. Due to this, the theory is not applicable for upstream locations for $(2F - 2/3) > 0$, and for downstream locations for $(2F - 2/3) < 0$. This limits the validity of the boundary layer theory, although the solutions in the incompressible limit themselves do not have any singularities or other abnormal features. The limit is due to the requirement that the variation in the volume fraction ϕ' has to be small compared with 1 for the expansion in (3.19).

7. Discussion

A Reynolds number for the flow can be defined more precisely from (3.21). The ratio of the inertial term on the left and the divergence of the stress on the right-hand side of the equation scales as $(\rho h^3/L\mathscr{B})$. This can be written as $Re(h/L)$, where the Reynolds number Re is

$$Re = \frac{\rho h^2}{\mathscr{B}}. \tag{7.1}$$

The Reynolds number increases proportional to h^2 as the layer height is increased, and it decreases as the Bagnold coefficients increase. In contrast to the flow of Newtonian fluids, the Reynolds number does not depend on the flow velocity. This is because the 'viscous' term on the right-hand side of (3.21) is also a quadratic function of the flow velocity, in a manner similar to the inertial terms on the left. This is in contrast to a Newtonian fluid, where the inertial terms are quadratic in the velocity and the viscous terms are linear, resulting in the Reynolds number increasing proportional to the flow velocity. The Reynolds number also depends sensitively on the ratio of the Bagnold coefficients and their derivative with respect to volume fraction.

In order to obtain an equivalent of the Mach number, it is necessary to return to the mass conservation equation (3.7) to obtain a physical interpretation of the factor $(\Xi/\rho\Xi_\rho)$. The Mach number is defined as $Ma = (\bar{u}/c_s)$, where $\bar{u}$ is the average velocity, and $c_s = (\partial p/\partial\rho)^{1/2}$ is the sound velocity based on the derivative of pressure with respect to density at constant temperature. In the present analysis, $Ma \sim (\dot{\gamma}h/(\partial p/\partial\rho)^{1/2}) \sim (\dot{\gamma}h/\sqrt{\rho\Upsilon\Xi_\rho})$, where Υ is the scale for the granular temperature. Using $\Upsilon \sim d\dot{\gamma}$ when there is a balance between the shear production and inelastic dissipation, $\rho \sim (1/d^3)$, and $Re \sim (h^2/d^2\chi)$, we find that the ratio $(\Xi/\rho\Xi_\rho) \sim (Ma^2/Re)$. However, it should be noted that c_s is not the true sound speed, since the hydrodynamic modes in a dense sheared granular flow are qualitatively different from those in normal fluids (Kumaran 2009*c*). Due to this, the classical definition of the Mach number is of limited practical utility. A more useful dimensionless group is the ratio of the volume fraction variation and the mean volume fraction, referred to as the 'Compressibility number' $Co = Ma^2/Re$, which is a measure of the compressibility of the system. The flow can be considered incompressible (constant volume fraction) for $Co \ll 1$, while it is necessary to incorporate volume fraction variations for $Co \sim 1$. From (3.20), the Compressibility number can be precisely defined as $(\bar{B}_{yy}/\bar{\phi}\bar{B}_{\phi yy})$.

The development length $LL^*_{0.99}$ for flow development was defined as the length at which the height-averaged mean square difference between the developing and

https://doi.org/10.1017/jfm.2014.412 Published online by Cambridge University Press

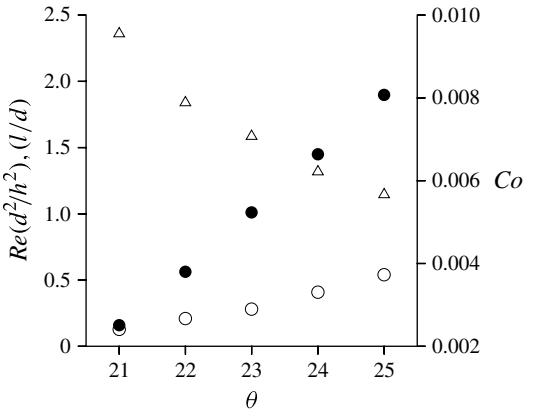


FIGURE 11. The product $Re(d^2/h^2)$ (○) and the ratio (l/d) (△) on the left y axis; and the compressibility number $Co = (\bar{B}_{yy}/\bar{\phi}\bar{B}_{\phi yy})$ (●) on the right y axis as a function of angle of inclination in degrees for the flow down an inclined plane considered by Kumaran & Maheshwari (2012).

Bagnold profiles is 0.01 times the mean velocity. Here, $L = Re\,h$ from (4.27), and (4.30) is used for defining $L^*_{0.99}$. The Reynolds numbers and the lengths cannot be directly estimated from the expressions for the Bagnold coefficients, since the variations of the Bagnold coefficients with volume fraction are required. If the Bagnold coefficients are assumed to be of the form $B_{ij} \sim (\phi_{ad} - \phi)^{-\alpha}$, where ϕ_{ad} is the volume fraction for dynamical arrest, the factor $\mathscr{B} = (\bar{B}_{xy} - \bar{B}_{\phi xy}\bar{B}_{yy}/\bar{B}_{\phi yy})$ in the expressions (4.27) and (5.6) is identically zero. It is necessary to use a more detailed functional form for the Bagnold coefficients to determine the leading non-zero contribution to the factor $\mathscr{B}$. However, simulation results for the unsteady fully developed flow down an inclined plane (Kumaran & Bharathraj 2013) can be used to extract the necessary length scales. In that analysis, it was shown that the characteristic time scale for the flow development, τ, was given by

$$\tau = \left(\frac{\rho h^3 \bar{B}_{xy}}{4 g_x}\right)^{1/2} \mathscr{B}^{-1}. \tag{7.2}$$

Using this, the Reynolds number can be expressed in terms of τ,

$$Re = \frac{L}{h} = \tau \left(\frac{4\rho g_x h}{\bar{B}_{xy}}\right)^{1/2}. \tag{7.3}$$

Since the Reynolds number increases proportional to h^2 in (7.1), it is convenient to provide results for the product $(Re\,d^2/h^2)$. This is shown as a function of the angle of inclination for the flows considered by Kumaran & Maheshwari (2012) in figure 11. The product $Re(d^2/h^2)$ varies from approximately 0.13 at the lowest angle of inclination $\theta = 21^\circ$ for a steady flow, to a maximum of approximately 0.53 at $\theta = 25^\circ$. The length $l = \sqrt{2\mathscr{B}/\bar{\rho}}$ in the expression for the boundary layer thickness can be expressed in terms of the relaxation time as $l = ((1/\tau)(h^3\bar{B}_{xy}/\bar{\rho}g_x)^{1/2})^{1/2}$. This length varies between 1 and 2.5 particle diameters when the angle of inclination is varied from 21 to 25°, and it increases approximately linearly in this range, as shown in figure 11.

https://doi.org/10.1017/jfm.2014.412 Published online by Cambridge University Press

(h/d)	Angle (deg.)	$Re = (L/h)$	$(LL^*_{0.99}/h)\|_{\beta=0}$	$(LL^*_{0.99}/h)\|_{\beta=1}$	$(LL^*_{0.99}/h)\|_{\beta=10}$
5	21	3.18	0.436	2.62	104.07
5	25	13.49	1.71	11.15	442.31
20	21	50.79	6.974	41.98	1665.14
20	25	215.89	27.41	178.45	7077.02
50	21	317.45	43.59	262.40	10 407.17
50	25	1349.30	171.33	1115.33	44 231.41
100	21	1269.81	174.34	1049.62	41 628.62
100	25	5397.23	685.33	4461.33	176 926.23

TABLE 1. The variation of the Reynolds number and the scaled flow development length $(LL^*_{0.99}/h)$ with the ratio of layer height and particle diameter for two different angles of inclination for the flow configuration of Kumaran & Maheshwari (2012).

Table 1 shows the Reynolds number and (L/h) for the two extreme angles of inclination for a stable flow, 21 and 25°, in the simulations of Kumaran & Maheshwari (2012). It is observed that the Reynolds number is $O(1)$ only for smallest heights that are comparable with the particle diameter. It should be noted that an analysis based on the Bagnold law will not be applicable to thin layers of height approximately five particle diameters or less, since energy conduction at the base and free surface are likely to be significant. So it appears that there is no low-Reynolds-number regime where the continuum theory can be applied, and all realistic flows with height a few tens of particle diameters are invariably high Reynolds number. This is because the Reynolds number does not depend on the velocity, but only on the layer height. Since the Reynolds number is always high for macroscopic flows, the shallow flow approximation $(h/L) \ll 1$ is a good one. Paradoxically, the shallow flow approximation becomes better as the layer height increases, because the (h/L) decreases proportional to (d^2/h^2). Table 1 also reflects the strong dependence of $L^*_{0.99}$ on the base roughness. The development length $LL^*_{0.99}$ is relatively small for a frictional base with a no-slip boundary condition ($\beta = 0$). If we consider particles of diameter 1 mm, the development length is approximately 14 cm for $\theta = 21°$, and approximately 54 cm for $\theta = 25°$ for a layer with height equal to 20 particle diameters. For a slip base with $\beta = 10$, the development length increases dramatically to 33 m at $\theta = 21°$, and 154 m at $\theta = 25°$ for a layer of height 20 particle diameters. This indicates that base slip could have a significant effect on the development length.

The compressibility number, $(\bar{B}_{yy}/\bar{\phi}\bar{B}_{\phi yy})$, can also be evaluated from the data of Kumaran & Maheshwari (2012) for the disordered flow. A very good fit for the Bagnold coefficient data of Kumaran & Maheshwari (2012) is observed using a relation of the type $B_{ij} = B^{\dagger}_{ij}(\phi_{ad} - \phi)^{-2}$, where $\phi_{ad} = 0.593$, and the coefficients $B^{\dagger}_{xy} = 0.0122$ and $B^{\dagger}_{yy} = 0.0265$, as shown in figure 12. Using this fitting form, the compressibility number $(\bar{B}_{yy}/\bar{\phi}\bar{B}_{\phi yy}) = 2\bar{\phi}^{-1}(\phi_{ad} - \bar{\phi})^{-1}$. This compressibility number is plotted as a function of volume fraction in figure 12, and as a function of angle of inclination in figure 11. The compressibility number decreases as the volume fraction increases or the angle of inclination decreases, from approximately 0.01 at $\theta = 25°$ to 0.0025 at $\theta = 21°$. This shows why the constant volume fraction approximation is a very good approximation for dense granular flows of the type studied by Maheshwari & Kumaran (2012).

https://doi.org/10.1017/jfm.2014.412 Published online by Cambridge University Press

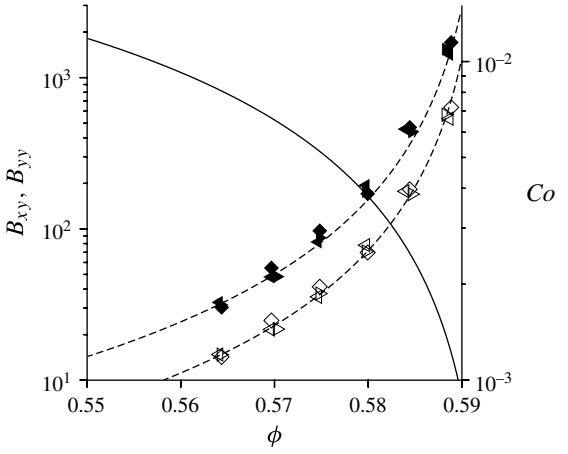


FIGURE 12. The Bagnold coefficients $B_{xy}(\phi)$ (open symbols) and $B_{yy}(\phi)$ (filled symbols) as a function of volume fraction for the disordered flow as reported by Kumaran & Maheshwari (2012) for a system with height approximately 37 particle diameters, and for the ratio of base and moving particle diameters 0.62 (◁), 0.75 (▷) and 1.0 (◇); and the compressibility number $Co = (\bar{B}_{yy}/\bar{\phi}\bar{B}_{\phi yy})$ as a function of volume fraction (solid line, right y axis). The dashed lines show the fit $B_{xy} = 0.0122/(\phi_{ad} - \phi)^2$ and $B_{yy} = 0.0265/(\phi_{ad} - \phi)^2$, where $\phi_{ad} = 0.593$.

Acknowledgements

The author would like to thank the Department of Science and Technology, Government of India, for financial support. A part of the research work was carried out at the Kavli Institute of Theoretical Physics, University of California, Santa Barbara, USA during the research program on Fluid-Mediated Particle Transport in Geophysical Flows. This research was supported in part by the National Science Foundation under grant no. NSF PHY11-25915.

Appendix A. Governing equations incorporating height variation

Using the transformation (3.31), then (3.23) and (3.24) become

$$u_y = h\left(\frac{\partial u_x}{\partial y^*}\right)^{-1}\left[-u_x\frac{\partial u_x}{\partial x} + g_x + \frac{g_y\bar{B}_{xy}}{\bar{B}_{yy}}\right] + y^* u_x\frac{\mathrm{d}h}{\mathrm{d}x} + (h^2\rho)^{-1}\frac{\partial}{\partial y^*}\left(\mathscr{B}\left|\frac{\partial u_x}{\partial y^*}\right|\right). \quad (A\,1)$$

This can be inserted into the mass conservation equation, (3.13), to obtain a partial differential equation for u_x,

$$\frac{\partial u_x}{\partial x} - \frac{y^*}{h}\frac{\mathrm{d}h}{\mathrm{d}x}\frac{\partial u_x}{\partial y^*} + \frac{1}{h}\frac{\partial u_y}{\partial y^*} + \frac{1}{\bar{\phi}}\left(\frac{\partial}{\partial x} - \frac{y^*}{h}\frac{\mathrm{d}h}{\mathrm{d}x}\frac{\partial}{\partial y^*}\left(u_x\left(\frac{h\displaystyle\int_0^1 \mathrm{d}y'\rho g_y}{(\bar{B}_{\phi yy}/h^2)(\partial u_x/\partial y')^2} - \frac{\bar{B}_{yy}}{\bar{B}_{\phi yy}}\right)\right)\right.$$
$$\left. + \frac{1}{h}\frac{\partial}{\partial y^*}\left(u_y\left(\frac{h\displaystyle\int_0^a \mathrm{d}y'\rho g_y}{(\bar{B}_{\phi yy}/h^2)(\partial u_x/\partial y')^2} - \frac{\bar{B}_{yy}}{\bar{B}_{\phi yy}}\right)\right)\right) = 0. \quad (A\,2)$$

https://doi.org/10.1017/jfm.2014.412 Published online by Cambridge University Press

The boundary conditions are the zero penetration and the generalised slip model at the bottom surface $y^* = 0$, discussed in more detail in § 4,

$$u_y = 0 \tag{A 3}$$

$$u_x = \beta \frac{\partial u_x}{\partial y^*} \tag{A 4}$$

where β is a dimensionless slip length. The kinematic condition at the top surface, $y^* = 1$, relates the change in height to the tangential and normal velocities. At steady state, the kinematic condition reduces to

$$u_x \frac{\mathrm{d}h}{\mathrm{d}x} = u_y. \tag{A 5}$$

The zero shear stress condition at $y^* = 1$ is

$$\frac{\partial u_x}{\partial y^*} = 0. \tag{A 6}$$

The equation for the stream function (3.22), expressed in terms of y^* and using the transformation (3.31),

$$\frac{\bar{\rho} h^3}{\mathscr{B}} \left(\frac{\partial \psi}{\partial y^*} \frac{\partial^2 \psi}{\partial x \partial y^*} - \frac{\partial \psi}{\partial x} \frac{\partial^2 \psi}{\partial y^{*2}} \right) - \frac{\bar{\rho} h^2}{\mathscr{B}} \frac{\mathrm{d}h}{\mathrm{d}x} \left(\frac{\partial \psi}{\partial y^*} \right)^2 = \frac{\partial}{\partial y^*} \left(\left(\frac{\partial^2 \psi}{\partial y^{*2}} \right)^2 \right). \tag{A 7}$$

The zero shear and normal velocity conditions at the bottom surface $y^* = 0$, (A 4), expressed in terms of the stream function, are

$$\frac{\partial \psi}{\partial x} = 0 \tag{A 8}$$

$$\frac{\partial \psi}{\partial y^*} = \beta \frac{\partial^2 \psi}{\partial y^{*2}} \tag{A 9}$$

while the kinematic condition (A 5) and the zero stress condition (A 6) at $y^* = 1$ are

$$\frac{1}{h} \frac{\partial \psi}{\partial y^*} \frac{\mathrm{d}h}{\mathrm{d}x} = -\frac{\partial \psi}{\partial x} + \frac{y^*}{h} \frac{\partial \psi}{\partial y^*} \frac{\mathrm{d}h}{\mathrm{d}x} \tag{A 10}$$

$$\frac{\partial \psi}{\partial x} = 0 \tag{A 11}$$

$$\frac{\partial^2 \psi}{\partial y^{*2}} = 0. \tag{A 12}$$

The conditions (A 10) and (A 11) turn out to be identical, and also identical to the constant volumetric flow rate condition. Since the difference in the stream function between two locations is equal to the volumetric flow rate between those two locations, and the stream function has been set equal to zero at $y^* = 0$, it follows that the stream function at $y^* = 1$ has to be independent of x.

Appendix B. Solution or eigenvalue problem for developing flow

The (4.26) can be solved using the separation-of-variables procedure, by expressing

$$\psi'(x^\dagger, y^\dagger) = \sum_i A_i X_i(x^\dagger) Y_i(y^\dagger). \tag{B 1}$$

https://doi.org/10.1017/jfm.2014.412 Published online by Cambridge University Press

The height perturbation h' can then be expressed using kinematic condition (4.18),

$$\frac{h'}{\bar{h}} = -\sum_i \frac{A_i}{\bar{u}\bar{h}(5/3+5\beta/2)} X_i(x^\dagger) Y_i(y^\dagger = 1). \tag{B 2}$$

The equations for $X_i(x^\dagger)$ and $Y_i(y^\dagger)$ are

$$\frac{\mathrm{d}X_i}{\mathrm{d}x^\dagger} + \alpha_i X_i = 0, \tag{B 3}$$

$$\mathscr{L}^{(1)} Y_i + \alpha_i \mathscr{L}^{(2)} Y_i = 0, \tag{B 4}$$

where the linear operators $\mathscr{L}^{(1)}$ and $\mathscr{L}^{(2)}$ are

$$\mathscr{L}^{(1)} = 2\frac{\mathrm{d}}{\mathrm{d}y^\dagger}\left(\frac{\mathrm{d}\bar{u}^*}{\mathrm{d}y^\dagger}\frac{\mathrm{d}^2}{\mathrm{d}y^{\dagger 2}}\right), \tag{B 5}$$

$$\mathscr{L}^{(2)} = \left(\bar{u}^*\frac{\mathrm{d}}{\mathrm{d}y^\dagger} - \frac{\mathrm{d}\bar{u}^*}{\mathrm{d}y^\dagger}\right). \tag{B 6}$$

Equation (B 4), subject to the boundary conditions, the zero normal velocity and the slip condition (equivalent of (4.6)) at the base

$$Y_i = 0 \quad \text{at } y^\dagger = 0 \tag{B 7}$$

$$\frac{\mathrm{d}Y_i}{\mathrm{d}y^\dagger} = \beta\frac{\mathrm{d}^2 Y_i}{\mathrm{d}y^{\dagger 2}} \quad \text{at } y^\dagger = 0, \tag{B 8}$$

and the zero shear stress condition (equivalent of (4.5)) at the top

$$\frac{\mathrm{d}^2 Y_i}{\mathrm{d}y^{\dagger 2}} = 0 \quad \text{at } y^\dagger = 1, \tag{B 9}$$

constitute an eigenvalue problem for the discrete eigenvalues α_i.

The discrete eigenvalues are shown as a function of β in figure 13. It is observed that the eigenvalues are well separated; the first eigenvalue is between one and two orders of magnitude smaller than the second. This indicates that the 'ground state dominance' observed for the time evolution of an unsteady flow (Kumaran & Bharathraj 2013) is also present for the spatial flow development, and it may be sufficient to approximate the profile by just the first eigenfunction due to the rapid decay rate of the higher eigenfunctions. The eigenvalues decrease as β is increased, and there is a decrease by three orders of magnitude when β increases from zero to ten. The first eigenvalue decreases proportional to β^{-2} for $\beta \gg 1$, while the higher eigenvalues decay proportional to β^{-1}. Therefore, the spatial relaxation rate to the fully developed profile is much slower as the slip velocity at the base increases. The first three eigenfunctions are shown as a function of height in figure 14 for four different values of the slip parameter β, for a specific normalisation $(\mathrm{d}^2 Y_i/\mathrm{d}y^{\dagger 2}) = 1$ at $y^\dagger = 0$. All of the eigenfunctions have a similar variation near $y^\dagger = 0$ due to the boundary conditions (B 7) and (B 8) and the normalisation condition; in the limit $y^\dagger \to 0$, the analytical approximation for the eigenfunctions is $Y_i \approx (y^\dagger/\beta) + (y^{\dagger 2}/2)$. The lowest eigenfunction increases nearly linearly with $y^\dagger$ for $y^\dagger \to 1$, while the higher eigenfunctions remain bounded.

The adjoint problem can be evaluated by multiplying (B 4) by the adjoint function $V(y^\dagger)$ and integrating over $y^\dagger$,

$$\mathscr{L}^{(1)*} V + \alpha \mathscr{L}^{(2)*} V = 0, \tag{B 10}$$

https://doi.org/10.1017/jfm.2014.412 Published online by Cambridge University Press

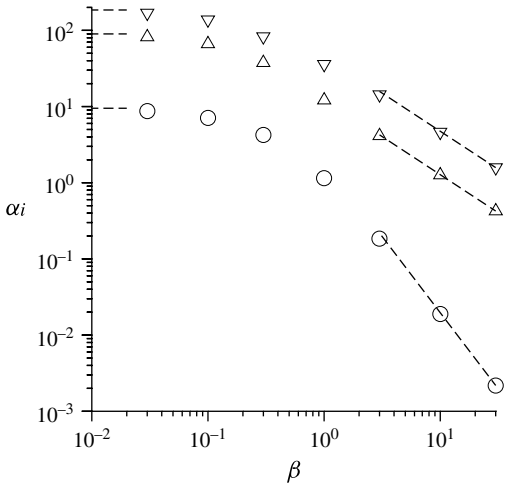


FIGURE 13. The first (○), second (△) and third (▽) eigenvalues in the order of increasing magnitude as a function of the scaled slip length β. The dashed lines on the left provide the value for $\beta = 0$, and the dashed line on the right indicates a slope of -2 for the first eigenvalue and a slope of -1 for the second and third eigenvalues on the log–log graph.

with boundary conditions

$$V = \beta \frac{\mathrm{d}V}{\mathrm{d}y^\dagger} \quad \text{at } y^\dagger = 0, \tag{B 11}$$

$$\frac{\mathrm{d}V}{\mathrm{d}y^\dagger} = 0 \quad \text{at } y^\dagger = 1, \tag{B 12}$$

$$\frac{\mathrm{d}}{\mathrm{d}y^\dagger}\left(\sqrt{1-y^\dagger}\frac{\mathrm{d}V}{\mathrm{d}y^\dagger}\right) + \alpha\left(\frac{1}{3}+\frac{\beta}{2}\right) = 0 \quad \text{at } y^\dagger = 1, \tag{B 13}$$

where

$$\mathscr{L}^{(1)*} = 2\frac{\mathrm{d}\bar{u}_x^*}{\mathrm{d}y^\dagger}\frac{\mathrm{d}^3}{\mathrm{d}y^{\dagger 3}} + 4\frac{\mathrm{d}^2\bar{u}_x^*}{\mathrm{d}y^{\dagger 2}}\frac{\mathrm{d}}{\mathrm{d}y^{\dagger 2}} + 2\frac{\mathrm{d}^3\bar{u}_x^*}{\mathrm{d}y^{\dagger 3}}\frac{\mathrm{d}}{\mathrm{d}y^\dagger}, \tag{B 14}$$

$$\mathscr{L}^{(2)*} = \bar{u}_x^*\frac{\mathrm{d}}{\mathrm{d}y^\dagger} + 2\frac{\mathrm{d}\bar{u}_x^*}{\mathrm{d}y^\dagger}. \tag{B 15}$$

The solutions for V_i (B 10) which satisfy the boundary conditions (B 11)–(B 13) are shown in figure 14 for a specific normalisation condition $V_i = 1$ at $y^\dagger = 0$.

The orthogonality relations can be determined as follows. The inner product is defined as

$$\langle V_j, Y_i\rangle = \int_0^1 \mathrm{d}y^\dagger V_j(y^\dagger) Y_i(y^\dagger). \tag{B 16}$$

If we take the inner product of (B 4) with the eigenfunction V_j for the adjoint problem, we obtain

$$\langle V_j, \mathscr{L}^{(1)} Y_i\rangle + \alpha_i \langle V_j, \mathscr{L}^{(2)} Y_i\rangle = 0. \tag{B 17}$$

Using integration by parts, this equation can be written as

$$(\alpha_i - \alpha_j)\langle V_j, \mathscr{L}^{(2)} Y_i\rangle = 0. \tag{B 18}$$

https://doi.org/10.1017/jfm.2014.412 Published online by Cambridge University Press

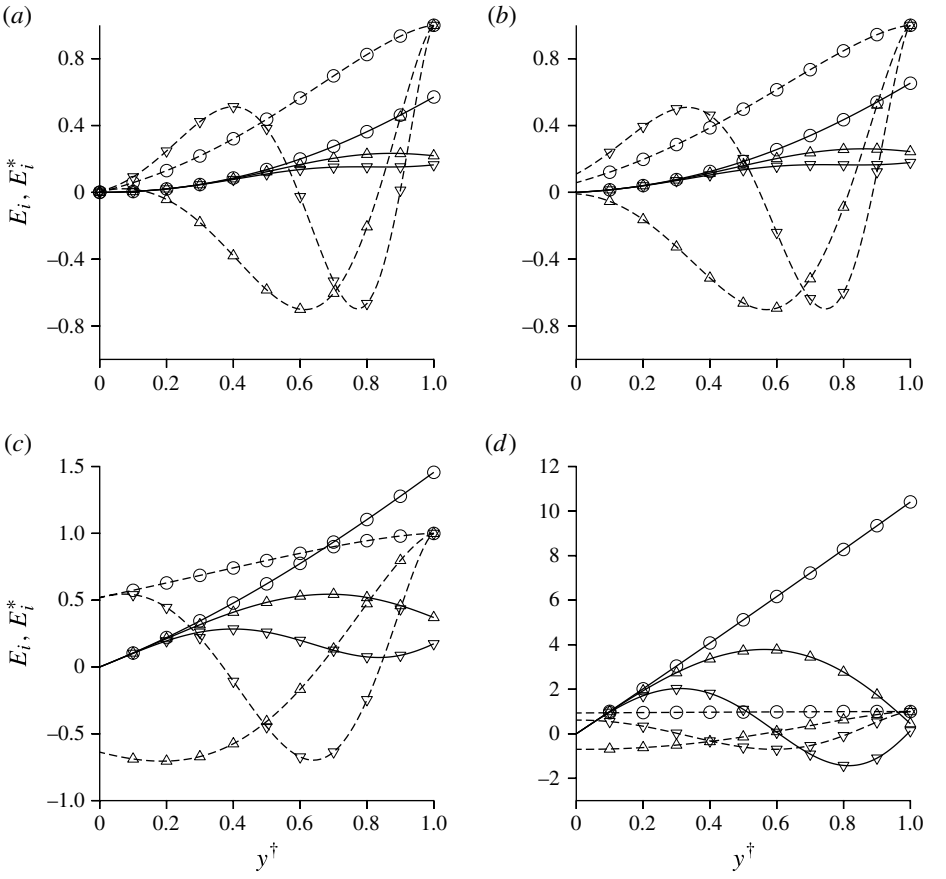


FIGURE 14. The solutions $Y_i(y^\dagger)$ of (B 4) (solid lines) and $V_i(y^\dagger)$ of (B 10) (dashed lines) corresponding to the lowest eigenvalue α_1, (○), the next higher eigenvalue α_2 (△), and the next higher eigenvalue α_3 (▽) for $\beta = 0$ (*a*), 0.1 (*b*), 1 (*c*) and 10 (*d*). In the solutions, the normalisation used is $(\mathrm{d}^2 Y_i/\mathrm{d}y^{\dagger 2}) = 1.0$ at $y^\dagger = 0$, and $V_i = 1$ at $y^\dagger = 1$.

For $i \neq j$, the orthogonality relation reduces to

$$\langle V_j, \mathscr{L}^{(2)} Y_i \rangle = 0. \tag{B 19}$$

The solution for the stream function, (B 1), can be expressed as

$$\psi'(x^\dagger, y^\dagger) = \sum_i A_i' \exp(-\alpha_i x^\dagger) Y_i(y^\dagger) + \psi_B', \tag{B 20}$$

where the stream function for the Bagnold profile, obtained by integrating the velocity profile (4.7) with the condition $\psi_B'(y^\dagger) = 0$ at $y^\dagger = 0$, is

$$\psi_B'(x^\dagger, y^\dagger) = \bar{u}h \left(\frac{2(1-y^\dagger)^{5/2}}{3} - \frac{5y^\dagger}{3} \right) + \bar{u}_s h y^\dagger. \tag{B 21}$$

The inlet condition at $x^\dagger = 0$ is considered to be a plug flow with the same volumetric flow rate as the steady flow, $u_x = \bar{u} + \bar{u}_s$. For the plug flow, the stream function is

https://doi.org/10.1017/jfm.2014.412 Published online by Cambridge University Press

$\psi'_P(0, y^\dagger) = (\bar{u} + \bar{u}_s)hy^\dagger$, and the initial condition for the stream function is

$$\psi'_I(x^\dagger = 0, y^\dagger) = \psi'_P - \psi'_B = -\frac{2\bar{u}h}{3}\left((1-y^\dagger)^{5/2} + (y^\dagger - 1)\right). \tag{B 22}$$

The initial condition for the stream function can be expressed as

$$\sum_i A_i Y_i(y^\dagger) = \psi'_I(y^\dagger). \tag{B 23}$$

The coefficients A_i are determined from the orthogonality relation,

$$A_i = \frac{\langle V_i, \mathscr{L}^{(2)}\psi'_I\rangle}{\langle V_i, \mathscr{L}^{(2)}Y_i\rangle}. \tag{B 24}$$

In § 4.2 on the effect of compressibility on the velocity profiles, equation (4.35) can be solved to obtain u''_y in terms of u''_x,

$$u''_y = \left(\frac{\partial \bar{u}_x}{\partial y}\right)^{-1}\left[\frac{2\mathscr{B}}{\bar{\rho}}\frac{\partial}{\partial y}\left(\frac{\mathrm{d}\bar{u}_x}{\mathrm{d}y}\frac{\partial u''_x}{\partial y}\right) - \bar{u}_x\frac{\partial u''_x}{\partial x}\right]. \tag{B 25}$$

This is inserted into the mass conservation equation to obtain an equation for u''_x,

$$\frac{\partial u''_x}{\partial x} + \frac{\partial}{\partial y}\left[\left(\frac{\partial \bar{u}_x}{\partial y}\right)^{-1}\left[\frac{2\mathscr{B}}{\rho}\frac{\partial}{\partial y}\left(\frac{\mathrm{d}\bar{u}_x}{\mathrm{d}y}\frac{\partial u''_x}{\partial y}\right) - \bar{u}_x\frac{\partial u''_x}{\partial x}\right]\right] = -\frac{\bar{u}_x}{\bar{\phi}}\frac{\partial \phi'}{\partial x}. \tag{B 26}$$

Using $y^\dagger = (y/h)$ and the scaled x coordinate given in (4.27), equation (B 26) can be reduced to

$$\frac{\partial u''_x}{\partial x^\dagger} + \frac{\partial}{\partial y^\dagger}\left[\left(\frac{\partial \bar{u}^*_x}{\partial y^\dagger}\right)^{-1}\left[\frac{\partial}{\partial y^\dagger}\left(\frac{\mathrm{d}\bar{u}^*_x}{\mathrm{d}y^\dagger}\frac{\partial u''_x}{\partial y^\dagger}\right) - \bar{u}^*_x\frac{\partial u''_x}{\partial x^\dagger}\right]\right] = \frac{2\bar{B}_{yy}}{B_{\phi yy}}\frac{\bar{u}^*_x}{\bar{\phi}}\left(\frac{\partial \bar{u}^*_x}{\partial y^\dagger}\right)^{-1}\frac{\partial}{\partial x^\dagger}\left(\frac{\partial^2 \psi'}{\partial y^{\dagger 2}}\right), \tag{B 27}$$

where $\bar{u}^*_x$ is given in (4.24). This inhomogeneous equation is solved using the substitution (4.31) for ψ', and assuming u''_x is of the form

$$u''_x = \sum_i \exp(-\alpha_i x^\dagger) W_i(y^\dagger). \tag{B 28}$$

The differential equation for the functions $W_i(y^\dagger)$ are

$$\frac{\partial}{\partial y^\dagger}\left[\left(\frac{\partial \bar{u}^*_x}{\partial y^\dagger}\right)^{-1}\left[\frac{\partial}{\partial y^\dagger}\left(\frac{\mathrm{d}\bar{u}^*_x}{\mathrm{d}y^\dagger}\frac{\partial W_i}{\partial y^\dagger}\right) + \alpha_i \bar{u}^*_x\frac{\partial W_i}{\partial x^\dagger}\right]\right] - \alpha_i W_i = -\frac{2\alpha_i \bar{B}_{yy}}{B_{\phi yy}}\frac{\bar{u}^*_x}{\bar{\phi}}\left(\frac{\partial \bar{u}^*_x}{\partial y^\dagger}\right)^{-1}\left(\frac{\partial^2 Y_i}{\partial y^{\dagger 2}}\right). \tag{B 29}$$

The velocity u''_y in the y direction can be related to the function W_i using (B 25),

$$u''_y = \frac{2\mathscr{B}}{\rho}\left(\frac{\mathrm{d}\bar{u}^*_x}{\mathrm{d}y^\dagger}\right)^{-1}\sum_i \exp(-\alpha_i x^\dagger)\left[\frac{\mathrm{d}}{\mathrm{d}y^\dagger}\left(\frac{\mathrm{d}\bar{u}^*_x}{\mathrm{d}y^\dagger}\frac{\mathrm{d}W_i}{\mathrm{d}y^\dagger}\right) + \alpha_i \bar{u}^*_x W_i\right]. \tag{B 30}$$

https://doi.org/10.1017/jfm.2014.412 Published online by Cambridge University Press

The boundary conditions are the slip and zero normal velocity conditions at the base, and the zero shear stress condition at the top surface,

$$W_i = \beta \frac{\mathrm{d}W_i}{\mathrm{d}y^\dagger} \quad \text{at } y^\dagger = 0, \tag{B 31}$$

$$\frac{\mathrm{d}}{\mathrm{d}y^\dagger}\left(\frac{\mathrm{d}\bar{u}_x^*}{\mathrm{d}y^\dagger}\frac{\mathrm{d}W_i}{\mathrm{d}y^\dagger}\right) + \alpha_i \bar{u}_x^* W_i = \quad \text{at } y^\dagger = 0, \tag{B 32}$$

$$\frac{\mathrm{d}W_i}{\mathrm{d}y^\dagger} = 0 \quad \text{at } y^\dagger = 1. \tag{B 33}$$

REFERENCES

ALLEN, M. P. & TILDESLEY, D. J. 1992 *Computer Simulation of Liquids*. Clarendon Press.

BARAN, O., ERTAS, D., HALSEY, T. C., GREST, G. S. & LECHMAN, J. B. 2006 Velocity correlations in dense gravity-driven granular chute flow. *Phys. Rev.* E **74**, 051302.

BERZI, D. & JENKINS, J. T. 2011 Surface flows of inelastic spheres. *Phys. Fluids* **23**, 013303.

BREY, J. J., RUIZ-MONTERO, M. J. & MORENO, F. 2001 Hydrodynamics of an open vibrated granular system. *Phys. Rev.* E **63**, 061305; 061314.

CAMPBELL, C. S. 2002 Granular shear flows at the elastic limit. *J. Fluid Mech.* **465**, 261–291.

CAMPBELL, C. S. 2005 Stress-controlled elastic granular shear flows. *J. Fluid Mech.* **539**, 273–297.

CAMPBELL, C. S. 2011 Clusters in dense-inertial granular flows. *J. Fluid Mech.* **687**, 341–359.

CHIALVO, S., SUN, J. & SUNDARESAN, S. 2012 Bridging the rheology of granular flows in three regimes. *Phys. Rev.* E **85**, 021305.

COLE, D. M. & PETERS, J. F. 2007 A physically based approach to granular media mechanics: grain-scale experiments, initial results and implications to numerical modeling. *Granul. Matt.* **9**, 309–321.

COLE, D. M. & PETERS, J. F. 2008 Grain-scale mechanics of geologic materials and lunar simulants under normal loading. *Granul. Matt.* **10**, 171–185.

CUNDALL, P. A. & STRACK, O. D. L. 1979 A discrete numerical model for granular assemblies. *Geotechnique* **29**, 47–65.

ERTAS, D. & HALSEY, T. C. 2002 Granular gravitational collapse and chute flow. *Europhys. Lett.* **60**, 931–937.

GDR MIDI, 2004 On dense granular flows. *Eur. Phys. J.* E **14**, 341–365.

GRAY, J. M. N. T., WIELAND, M. & HUTTER, K. 1999 Gravity driven free surface flow of granular avalanches over complex basal topography. *Proc. R. Soc. Lond.* A **455**, 1841–1874.

HALSEY, T. C. 2009 Motion of packings of frictional grains. *Phys. Rev.* E **80**, 011303.

JENKINS, J. T. 2006 Dense shearing flows of inelastic disks. *Phys. Fluids* **18**, 103307.

JENKINS, J. T. 2007 Dense inclined flows of inelastic spheres. *Granul. Matt.* **10**, 47–52.

JENKINS, J. T. & RICHMAN, M. W. 1985 Grad's 13-moment system for a dense gas of inelastic spheres. *Arch. Rat. Mech. Anal.* **87**, 355–377.

JENKINS, J. T. & SAVAGE, S. B. 1983 A theory for the rapid flow of identical, smooth, nearly elastic particles. *J. Fluid Mech.* **130**, 186–202.

JOP, P., FORTERRE, Y. & POULIQUEN, O. 2006 A constitutive law for dense granular flows. *Nature* **441**, 727–730.

KHAKHAR, D. V., ORPE, A., ANDERSEN, P. & OTTINO, J. M. 2001 Surface flow of granular materials: model and experiments in heap formation. *J. Fluid Mech.* **441**, 255–264.

KUMARAN, V. 1998 Temperature of a granular material fluidised by external vibrations. *Phys. Rev.* E **57**, 5660–5664.

KUMARAN, V. 2004 Constitutive relations and linear stability of a sheared granular flow. *J. Fluid Mech.* **506**, 1–43.

KUMARAN, V. 2006*a* The constitutive relations for the granular flow of rough particles, and its application to the flow down an inclined plane. *J. Fluid Mech.* **561**, 1–42.

https://doi.org/10.1017/jfm.2014.412 Published online by Cambridge University Press

KUMARAN, V. 2006*b* Kinetic theory for the density plateau in the granular flow down an inclined plane. *Europhys. Lett.* **73**, 1–7.

KUMARAN, V. 2006*c* Velocity autocorrelations and the viscosity renormalisation in sheared granular flows. *Phys. Rev. Lett.* **96**, 258002.

KUMARAN, V. 2008 Dense granular flow down an inclined plane – from kinetic theory to granular dynamics. *J. Fluid Mech.* **599**, 120–168.

KUMARAN, V. 2009*a* Dynamics of dense sheared granular flows. Part I: structure and diffusion. *J. Fluid Mech.* **632**, 109–144.

KUMARAN, V. 2009*b* Dynamics of dense sheared granular flows. Part II: the relative velocity distribution. *J. Fluid Mech.* **632**, 145–198.

KUMARAN, V. 2009*c* Dynamics of a dilute sheared inelastic fluid. I. Hydrodynamic modes and the velocity correlation functions. *Phys. Rev.* E **79**, 011301.

KUMARAN, V. 2009*d* Dynamics of a dilute sheared inelastic fluid. II. The effect of correlations. *Phys. Rev.* E **79**, 011302.

KUMARAN, V. & BHARATHRAJ, S. 2013 The effect of base roughness on the development of a dense granular flow down an inclined plane. *Phys. Fluids* **25**, 070604.

KUMARAN, V. & MAHESHWARI, S. 2012 Transition due to base roughness in the dense granular flow down an inclined plane. *Phys. Fluids* **24**, 053302.

LAGREE, P.-Y., STARON, L. & POPINET, S. 2011 The granular column collapse as a continuum: validity of a two-dimensional Navier–Stokes model with a $\mu(I)$ rheology. *J. Fluid Mech.* **686**, 378–408.

LOUGE, M.-Y. 2003 Model for dense granular flows down bumpy surfaces. *Phys. Rev.* E **67**, 061303.

LOUGE, M.-Y. 2012 'Phonon' conductivity along a column of spheres in contact. *Granul. Matt.* **14**, 203–208.

LOUGE, M.-Y. & KEAST, S. C. 2001 On dense transition due to base roughness in the dense granular flow down an inclined plane. *Phys. Fluids* **24**, 053302.

LUN, C. K. K., SAVAGE, S. B., JEFFREY, D. J. & CHEPURNIY, N. 1984 Kinetic theories for granular flow: inelastic particles in Couette flow and slightly inelastic particles in a general flow field. *J. Fluid Mech.* **140**, 223–256.

MAHESHWARI, S. & KUMARAN, V. 2012 The effect of base dissipation on the granular flow down an inclined plane. *Granul. Matt.* **14**, 209–213.

ORPE, A. V. & KHAKHAR, D. V. 2007 Rheology of surface granular flows. *J. Fluid Mech.* **571**, 1–32.

ORPE, A. V., KUMARAN, V., REDDY, K. A. & KUDROLLI, A. 2008 Fast decay of the velocity autocorrelation function in dense shear flow of inelastic hard spheres. *Europhys. Lett.* **84**, 64003.

PEYNEAU, P.-E. & ROUX, J.-N. 2008 Frictionless bead packs have macroscopic friction, but no dilatancy. *Phys. Rev.* E **78**, 011307.

POULIQUEN, O. 1999 Scaling laws in granular flows down rough inclined planes. *Phys. Fluids* **11**, 542–548.

REDDY, K. A. & KUMARAN, V. 2007 Applicability of constitutive relations from kinetic theory for dense granular flows. *Phys. Rev.* E **76**, 061305.

REDDY, K. A. & KUMARAN, V. 2010 Dense granular flow down an inclined plane: a comparison between the hard particle model and soft particle simulations. *Phys. Fluids* **22**, 113302.

SAVAGE, S. B. & HUTTER, K. 1989 The motion of a finite mass of granular material down a rough incline. *J. Fluid Mech.* **199**, 177–215.

SAVAGE, S. B. & HUTTER, K. 1991 The dynamics of avalanches of granular materials from initiation to runout. Part I: analysis. *Acta Mechanica* **86**, 201–223.

SAVAGE, S. B. & JEFFREY, D. J. 1981 The stress tensor in a granular flow at high shear rates. *J. Fluid Mech.* **110**, 255–272.

SCHLICHTING, H. & GERSTEN, K. 2000 *Boundary-Layer Theory*. Springer.

SELA, N. & GOLDHIRSCH, I. 1998 Hydrodynamic equations for rapid flows of smooth inelastic spheres, to Burnett order. *J. Fluid Mech.* **361**, 41–74.

https://doi.org/10.1017/jfm.2014.412 Published online by Cambridge University Press

SELA, N., GOLDHIRSCH, I. & NOSKOWICZ, S. H. 1996 Kinetic theoretical study of a simply sheared two-dimensional granular gas to Burnett order. *Phys. Fluids* **8**, 2337–2353.

SENTHIL KUMAR, V. & KUMARAN, V. 2005 Voronoi cell volume distribution and configurational entropy of hard spheres. *J. Chem. Phys.* **123**, 114501.

SILBERT, L. E., ERTAS, D., GREST, G. S., HALSEY, T. C., LEVINE, D. & PLIMPTON, S. J. 2001 Granular flow down an inclined plane: Bagnold scaling and rheology. *Phys. Rev.* E **64**, 051302.

SOTO, R., MARESCHAL, M. & RISSO, D. 1999 Departure from Fourier's law for fluidized granular media. *Phys. Rev. Lett.* **83**, 5003–5006.

TORQUATO, S. 1995 Nearest neighbour statistics for packings of hard disks and spheres. *Phys. Rev.* E **51**, 3170–3182.

WALTON, O. R. 1993 Numerical simulation of inclined chute flows of monodisperse, inelastic, frictional spheres. *Mech. Mater.* **16**, 239–247.

WEINHART, T., THORNTON, A. R., LUDING, S. & BOKHOVE, O. 2012 Closure relations for shallow granular flows from particle simulations. *Granul. Matt.* **14**, 531–552.

https://doi.org/10.1017/jfm.2014.412 Published online by Cambridge University Press